Technical University of Munich
Physics Department

Bachelor Thesis

Analyses of Anisotropic Flow and Symmetry Planes Using Multiparticle Correlation Techniques in ALICE at the Large Hadron Collider

---

Author:
Alexander Frank

Supervisor & Advisor:
Prof. Dr. Laura Fabbietti
Dr. Ante Bilandzic

September 2016

Abstract

The study of collective anisotropic flow, a phenomenon where an initial state spacial anisotropy in the overlap region of two colliding nuclei gets transfered into a final state momentum space and particle production anisotropy, in ultrarelaticistic heavy-ion collisions proved to be one of the best probes to study in detail the properties of the strongly interacting matter created in such collisions, the quark-gluon plasma. To quantify the anisotropy in the particle momentum distribution a Fourier series is used whose coefficients v_n characterize flow magnitudes and whose phases Ψ_n represent symmetry planes, respectively in harmonic n.

In this thesis, after giving a brief introduction to quantum chromodynamics, heavy-ion collisions, quark-gluon plasma and the ALICE experiment, the latest method in measuring flow using Q-cumulants are introduced. Prerequisites like the mathematical description of flow, multiparticle correlations up to order 8 and the cumulant expansion are derived and with the combination of these techniques flow estimators which are able to suppress unwanted effects of nonflow are presented. It is shown how to analytically express these multiparticle correlation based estimators in terms of Q-vectors to drastically reduce computation time and it is discussed how they perform when not only collective flow is present. In the analysis part the obtained and implemented techniques are applied to data from the ALICE experiment at the CERN Large Hadron Collider, taken at energies of $\sqrt{s_{NN}} = 2.76\,\text{TeV}$ and $\sqrt{s_{NN}} = 5.02\,\text{TeV}$. All analyses are performed for both energies and compared for changes. The main object of study is the second Fourier coefficient v_2 representing elliptic flow, which is analyzed as a function of centrality, transverse momentum in the range $0.2 < p_{\mathrm{T}} < 5.0\,\text{GeV}/c$ and pseudorapidity in the range $|\eta| < 0.8$. Higher harmonic flow v_3, v_4, v_5 and v_6 are studied as a function of centrality. Finally correlations of symmetry planes are discussed and novel analytic observables which are free of flow coefficient contributions, exclusively measuring symmetry plane correlations on an event-per-event basis are introduced.

Contents

1 Introduction

1.1 Quantum Chromodynamics (QCD)

Quantum chromodynamics (QCD) is a type of quantum field theory, specifically a non-abelian gauge theory under the symmetry group SU(3). As part of the Standard Model of elementary particle physics it describes the strong interaction between quarks and gluons. Like the other fundamental interactions, the strong interaction is described by the exchange of gauge bosons (gluons), which arise from the invariance under local group transformations[1]. Similar to the electric charge in quantum electrodynamics (QED), particles interacting strongly have color charge which are, in analogy to additive color mixing, called red, green and blue (and their corresponding anti-color). Quarks carry only one unit of color charge (or anti-color charge), whereas gluons carry one unit of color as well as one unit of anti-color. This property stemming from the non-abelianity of QCD allows gluons in contrast to photons (the gauge bosons of QED) to couple to other gluons. These gluon-gluon interactions can constrain color fields and allow stringlike degrees of freedom (called color flux tubes or QCD strings) to form, which exert a constant force when stretched. This force is responsible for a property called *confinement*, meaning quarks are confined within color neutral structures and cannot be observed freely, since as two quarks get separated the energy density rises to a point where it becomes energetically favorable to create a quark anti-quark pair out of the vacuum, combining with the original quarks and thus creating two separated color neutral hadrons. Another important property of QCD is the *asymptotic freedom* [1, 2], which means that for large energies or small distances the interaction between quarks and gluons becomes asymptotically small and they behave like free particles. The reason for this is a dominance of anti-screening caused by virtual gluons over screening[2] caused by virtual quarks by a factor of 12 [4].

One can summarize QCD via its Lagrangian

$$\mathcal{L}_{\mathrm{QCD}} = \sum_q \bar{\psi}_{q,a} \left(i\gamma^\mu \partial_\mu \delta_{ab} - g_s \gamma^\mu t^C_{ab} \mathcal{A}^C_\mu - m_q \delta_{ab} \right) \psi_{q,b} - \frac{1}{4} F^A_{\mu\nu} F^{A\mu\nu}, \tag{1}$$

where Einstein notation is used, $\psi_{q,a}$ are the Dirac spinors for a quark field of flavor q and mass m_q with color-index a running from $a = 1$ to 3, γ_μ are the Dirac γ-matrices, $\mathcal{A}^C_\mu$ are the gluon fields with C running from $C = 1$ to 8, $t^C_{ab} \equiv \lambda^C_{ab}/2$ are the generators of the SU(3) group with λ^C_{ab} being the Gell-Mann matrices, g_s is the strong coupling constant and $F^A_{\mu\nu} = \partial_\mu \mathcal{A}^A_\nu - \partial_\nu \mathcal{A}^A_\mu - g_s f_{ABC} \mathcal{A}^B_\mu \mathcal{A}^C_\nu$ is the gluon's field strength tensor with the structure constant f_{ABC} of SU(3) defined by $[t^A, t^B] = i f_{ABC} t^C$ and δ_{ab} is the Kronecker delta [5]. Another term in the Lagrangian is allowed, which would be responsible for breaking of the CP-symmetry of QCD, leading to an electric-dipole moment of the neutron. Experiments have measured the coefficient $\bar{\theta}$ of this term to an upper bound of $\bar{\theta} < 10^{-11}$, which means QCD doesn't break CP-symmetry to our current knowledge and is known as the strong

---

[1] As QCD is a gauge theory, transformations between possible gauges form a Lie group (gauge group or symmetry group), which has a corresponding Lie algebra (namely the tangent space at the identity) with generators. Each group generator originates a gauge field to ensure the invariance of the Lagrangian under local group transformations (gauge invariance), the quanta of the fields being the gauge bosons.

[2] Screening means a phenomenon also present in QED, where a charge creates a vacuum polarization by attracting the opposingly charged particle of a virtual particle anti-particle pair and repelling the same charged one, effectively partially canceling the field of the charge. Anti-screening is not as easy to depict. For a qualitative explanation one can look e.g. at Peskin & Schroeder chapter 16.7 [3], but the important part is that instead of perturbations of the matter field inducing effective charges as in QED now perturbations in the gauge field induce dipoles which act exactly opposite to screening.

CP problem [6]. To study QCD one has to take into account the running[3] of the strong coupling $g_s^2/4\pi \equiv \alpha_s = \alpha_s(Q^2)$ making it only possible for large energies to use perturbative calculations (pQCD), which give good results for hard scattering processes [7]. For smaller energies ($\lesssim$ 1 GeV) non-perturbative methods have to be used, which are today mostly done via lattice calculations (LQCD) introduced by Wilson [8], where fields and interactions are simulated on discrete Wick rotated spacetime lattices and physical results are received as the limit for lattice spacing $a \to 0$. One has to note that since LQCD is based on the fundamental QCD Lagrangian all strong interaction dynamics are determined in terms of g_s and QCD can only give ratios of physical quantities [9]. To fix a dimensional scale the mass of a well known particle is inserted as given.

1.2 Quark-gluon Plasma (QGP)

The first statistical models of hadron thermodynamics were made, without knowledge of QCD and assuming thermalized matter, by Fermi [10], Hagedorn [11] and Landau [12], which already gave an upper limit for the temperature of hadronic matter. After the discovery of asymptotic freedom of QCD it was realized that it implies a transition to a new high temperature and high density phase of deconfined quarks and gluons [13, 14], which was named *quark-gluon plasma*[4] (QGP) by Edward Shuryak [15]. It was confirmed by SU(2) LQCD calculations [16–19] that this state of matter has a transition temperature which is experimentally observable by ultrarelativistic heavy-ion collisions (e.g. [20]).

One can depict the transition from hadronic matter to QGP in various simple models extending hadrons to structures made up of quarks and gluons. For example in a bag model [21] a pion gas is the dominant phase due to the bag pressure, which acts as a confining force binding quarks and gluons into hadrons. It results from the difference between the physical vacuum and the ground state in the deconfined phase. However for high temperatures the QGP is favored, because it has a higher number of intrinsic degrees of freedom [9]. This approach, as well as many others [22, 23], try to describe QGP by thermodynamics under some additional model assumptions. The more fundamental approach is to get strong interaction thermodynamics out of the fundamental strong interaction dynamics given by $\mathcal{L}_{\text{QCD}}$, which (at least today) mostly leads to LQCD.

Our current understanding of strongly interacting matter can be qualitatively summarized in a QCD phase diagram, which is shown in Fig. 1a) and Fig. 1b). At the origin of Fig. 1a) lies the vacuum. Also at zero temperature, but with a nonzero baryon chemical potential (which controls the density and is thus related to it) of about 1 GeV live nuclei and at even further densities properties of neutron stars are reached. For high densities, but low temperatures Fermi surfaces begin to exist and in analogy to the BCS (Bardeen–Cooper–Schrieffer) theory of superconductors [26] the color conducting phase can form coloured bosonic diquark pairs, the Cooper pairs of QCD, which can condense at low temperatures and form a color superconductor [27–29]. For low density and temperature the nucleons, i.e. protons and neutrons, behave like a gas, but as temperature and density are raised, the nucleons are excited into baryon resonances, which decay into pions and nucleons, altogether forming the hadron gas, which for even higher high temperature becomes the quark-gluon plasma. The transition starts as a first order transition from hadron gas to QGP for higher μ_B and ends in a critical point from where it becomes a continuous crossover for lower μ_B. The

---

[3] Because of screening and antiscreening described above the coupling becomes dependent on the transfered four-momentum squared Q^2, in short it *runs*.

[4] Plasma in general stands for matter where charges get screened by other mobile charges. In a QGP the confinement, resulting from anti-screening dominating screening, breaks for high temperatures due to thermal fluctuations of the gauge fields overcoming vacuum fluctuations.

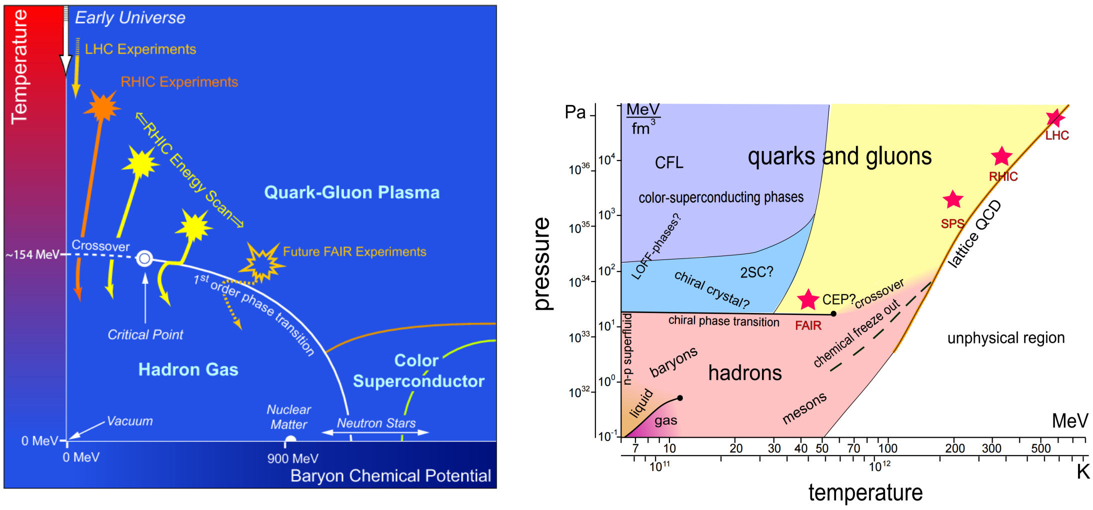

(a)

(b)

Figure 1: Schematic phase diagram of QCD in the temperature T - baryon chemical potential μ_B plane a) [24] and in the pressure p - temperature T plane b) [25].

most recent LQCD calculations [30, 31] show that the transition for small baryon chemical potential is not a clear phase transition, but an analytic crossover at a critical temperature of about $T_c = (154 \pm 9)$ MeV for $\mu_B = 0$. Also Fig. 1a) shows the evolution of a system created in heavy-ion collisions by the Large Hadron Collider (LHC) at CERN, the Relativistic Heavy Ion Collider (RHIC) in Brookhaven and the future Facility for Antiproton and Ion Research (FAIR) at the GSI. Starting right after the system is in approximate local thermal equilibrium after a collision with a temperature sufficient to create a QGP, cooling down, chemically freezing out and then kinetically freezing out. Similar conditions including the QGP are expected to have formed in the early Universe microseconds after the Big Bang, therefore understanding QGP properties helps understanding the evolution of the early Universe.

Contrary to the first anticipated picture of a weakly coupled system of quarks and gluons, experimental data of elliptic flow (which was consistent with predictions from ideal hydrodynamics), heavy quark suppression and jet quenching show that the QGP is strongly interacting (sQGP) [32–35]. The characteristic of an ideal fluid becomes important with new theoretical developments, in particular the Maldacena's conjecture[5] lead to gauge gravity dualities (AdS/CFT) allowing the study of certain strongly interacting theories with weakly interacting ones from string theory [36–38], stating that theories, which can be expressed by holographic duality have a lower bound on the shear viscosity over entropy ratio $\eta/s > \hbar/4\pi k_B$ [39, 40]. Current experiments show that the created QGP is very close to this boundary [41–44].

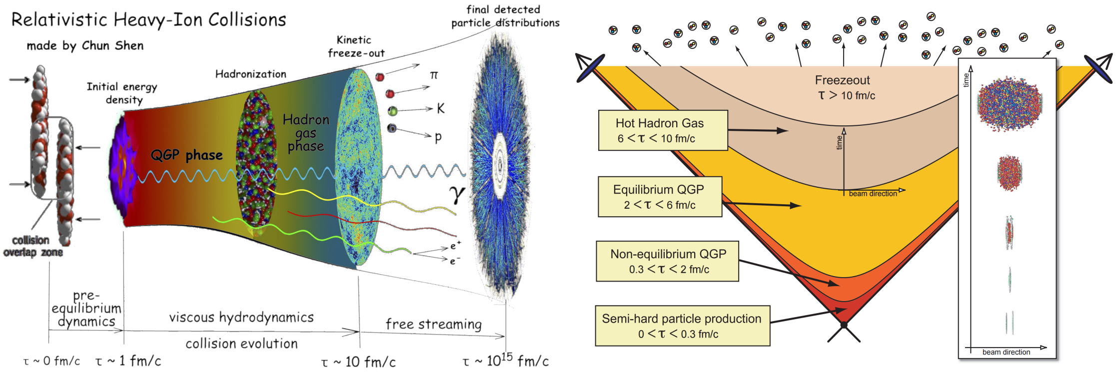

(a) (b)

Figure 2: Spacetime evolution of an ultrarelativistic heavy-ion collision depicting the different stages and the corresponding timescale. (a) from [45], b) from [46])

1.3 Heavy-Ion Collisions

To experimentally produce a system with temperatures above the strong phase transition temperature and create the QGP phase described in the previous section, ultrarelativistic heavy-ion collisions are the tool to go. As seen from the center of mass system each incoming nucleus can be considered as a Lorentz-contracted, coherent [47] cloud of partons, or in a more rigorous theoretical model as plates of color glass condensate (CGC) [48]. Roughly sketched the idea of CGC is as follows: Looking at an incident ion, as the collision energy increases the parton density also increases up to where the partons begin to overlap. Increasing the energy further leads to a saturation (parton recombination becomes favourable) and condensation of the “color drops” to a connected domain. The interaction time $\sim 1/\sqrt{s}$ [6] of two colliding ions is much shorter compared to the formation timescale of gluons so that they appear frozen, hence the term “glass”. The gluons are assumed to be coherend and therefore form classical fields which still lie on the Lorentz-contracted disc. When these two CGC discs collide they form a longitudinal (to the beam axis), classic colorfield, which is called glasma [49–51]. Through expansion this glasma becomes dilute and the single partons appear. Subsequent collisions between the partons then lead to local thermalization and the QGP is formed [9, 51]. Comparisons of experiments with hydrodynamic models assuming a perfect fluid show, that this has to happen in less than 1 fm/c [47]. Being nearly thermalized, the system evolves further under relativistic fluid dynamics, expanding, decreasing in energy density, cooling and finally hadronizing [51, 52]. These hadrons have at first enough energy to scatter elastically as well as inelastically, whereas inelastic scatterings can change the relative abundances of particle species while elastic collisions only change the momenta. When the energy per hadron does not allow any further inelastic processes, one speaks about the chemical freezeout. When also elastic processes stop the thermal or kinetic freezeout is reached. The produced hadrons free stream to the detectors which are discussed in the next chapter. The described evolution is shown in Fig. 2.

---

[5] Some string theories in curved space time are connected to conformal gauge theories in flat (3+1) dimensional space. In the limit of very strong coupling the string theory becomes identical to a version of Einstein's theory of general relativity with negative cosmological constant. In technical terms: 4 dimensional $N = 4$ Super Symmetric $SU(N_c)$ Yang Mills theory ($N_c = \infty$) is dual to Type II B Super String theory in an $AdS_5 \times S^5$ product space [36].

[6] Here s is one of the Mandelstam variables defined as $s = (p_1+p_2)^2$ with p_1 and p_2 beeing the 4-momenta of the colliding ions. For a collider experiment the 3-momenta $\overrightarrow{p_1}$ is equal to $-\overrightarrow{p_2}$ and $\sqrt{s}$ becomes the total center of mass energy.

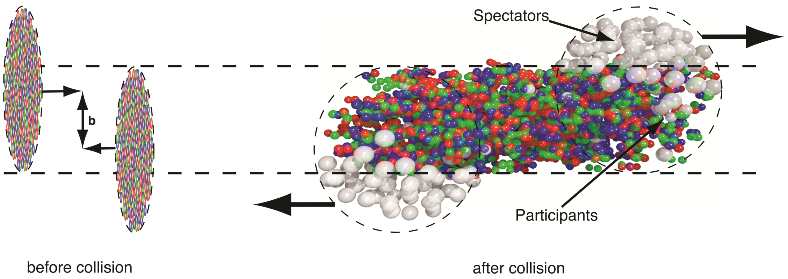

Figure 3: Left: Two ultrarelativistic heavy-ions before colliding with impact parameter $|\mathbf{b}|$. Right: Nuclei shortly after collision, the spectators proceed unaffected while the participants are responsible for particle production [53].

1.3.1 Centrality and Glauber Model

Heavy-ions are extended objects, and hence the system created in peripheral collisions will be different than the one created in head-on (central) collisions. It is therefore convenient to classify collisions by their *centrality* which is defined by the impact parameter $|\mathbf{b}|$. The impact parameter describes the length of the vector connecting the two nuclei centers projected onto a plane transverse to the beam axis and is not a direct experimental observable (see Fig. 3 left). However, the collision centrality can be inferred by assuming that the measured particle multiplicity M is a monotonic function of $|\mathbf{b}|$ [52, 53]. High multiplicity events stem from central collisions (small $|\mathbf{b}|$) and low multiplicity events from peripheral. If the particle multiplicity distribution dN/dM is measured event-by-event, one can define centrality classes by binning the distribution as fractions of its total integral [54]. For example an event i is in the centrality class 5–10%, which corresponds to central collisions, if its multiplicity M_i fulfills $N_{05} < M_i < N_{10}$, where the bin boundaries N_{05} and N_{10} are defined via

$$\frac{\int_{\infty}^{N_{05}} \frac{dN}{dM} dM}{\int_{\infty}^{0} \frac{dN}{dM} dM} = 0.05 \qquad \text{and} \qquad \frac{\int_{\infty}^{N_{10}} \frac{dN}{dM} dM}{\int_{\infty}^{0} \frac{dN}{dM} dM} = 0.1\,. \tag{2}$$

A commonly used model in relativistic heavy-ion physics to calculate geometric quantities is the *Glauber model*. With its help a set of parameters can be calculated, under the assumption that the collision of two nuclei can be seen as the superposition of the individual interactions of the constituent nucleons, which then also characterize the centrality. This set includes the number of participating nucleons N_{part} (nucleons which undergo at least one inelastic nucleon-nucleon collision) and the number of binary collisions N_{coll} (total number of inelastic nucleon-nucleon collisions, including multiple collisions of the same nucleon). N_{part} is also called number of *wounded* nucleons, wheres the nucleons which are not colliding are called *spectators*. Since the energies in relativistic heavy-ion collisions exceed the binding energy of the nuclei by a few orders of magnitude, the nucleus can be described by the spatial density distribution of the nucleons, which is parametrized as a Woods-Saxon distribution

$$\rho(r) = \rho_0 \cdot \frac{1 + wr^2/R^2}{1 + \exp\left(\frac{r-R}{a}\right)}\,. \tag{3}$$

Here ρ_0 is the density in the central region of the nucleus, R is the mean radius of the nucleus (at $\rho = 0.5\rho_0$), a characterizes the thickness of the surface layer and ω characterizes deviations from a sphere [52, 55]. These parameters[7] can be determined via electron

---

[7] If A is the number of nucleons in a nucleus, the mean electromagnetic radius is about $R \approx 1.2A^{1/3}$ fm

scattering in separate experiments. Another input to the Glauber model is the inelastic nucleon-nucleon cross section σ_{NN}, which can be measured in proton-proton collisions and includes the beam energy dependence of the model. With these conditions one can either proceed analytically under some further assumptions in the *optical-limit approximation* or numerically with a *Glauber Monte Carlo* approach.

The optical limit approach assumes that at sufficiently high energies as in relativistic collisions the nucleons carry enough momentum to stay undeflected on straight trajectories as the nuclei pass through each other. Furthermore it is assumed that nucleons move independently inside the nucleus and its size is large compared to the nucleon-nucleon interaction range [54]. These assumptions allow the derivation of analytic expressions for $\sigma_{NucleusNucleus}$, N_{coll}, N_{part} expressed in the independently measured quantities $\rho(r)$ and σ_{NN}.[8]

The Monte Carlo approach is a straightforward algorithm working as follows: 1. sample the nucleons in the nucleus following the probability distribution defined in Eq. (3); 2. chose a random impact parameter $|\mathbf{b}|$ from the distribution $d\sigma/db = 2\pi b$, 3. (since it is assumed that the nucleons travel on straight trajectories and σ_{NN} is independent of the number of collisions underwent before) in the simplest version of the algorithm, tag the nucleon and count the number of collisions if the transverse separation of two nucleons is less than $\sqrt{\sigma_{NN}/\pi}$. By repeating this procedure for a sufficient number of times, a relation between N_{coll} and N_{part} can be calculated.

To relate the experimentally measured multiplicity to N_{coll} and N_{part} from simulation, a simple model to simulate the particle production for a set of events generated by the Glauber MC method has to be used. The obtained multiplicity distribution can then be fitted to the experimental one (see fig. 12) and also binned in the same way as the experimental one. Since the mean values of the simulation parameters, e.g. $\langle b \rangle$ or $\langle N_{coll} \rangle$, are known per bin of simulated multiplicity, it can now be assumed that the mean quantities are also valid for the experimental distribution [54].

A different way of determining the centrality instead of measuring the multiplicity is by measuring the spectators unaffected by the collision in a Zero Degree Calorimeter (ZDC), assuming again a monotonic dependence for the deposited energy as a function of $|\mathbf{b}|$. In particular, larger $|\mathbf{b}|$ leads to more spectators and hence more energy deposited in the ZDC. Both methods can be combined to decrease uncertainties.

However in general there is no standard way of defining centrality classes and different experiments use different techniques and frameworks. Since the data used in this work comes from the ALICE experiment it is referred to [56] for a more detailed description.

---

and the central density about $\rho_0 \approx 0.17$ nucleons/fm^3 [55].

[8] For a more in depth description see [54] or more specific to ALICE [56].

2 Experimental Setup

2.1 Large Hadron Collider (LHC)

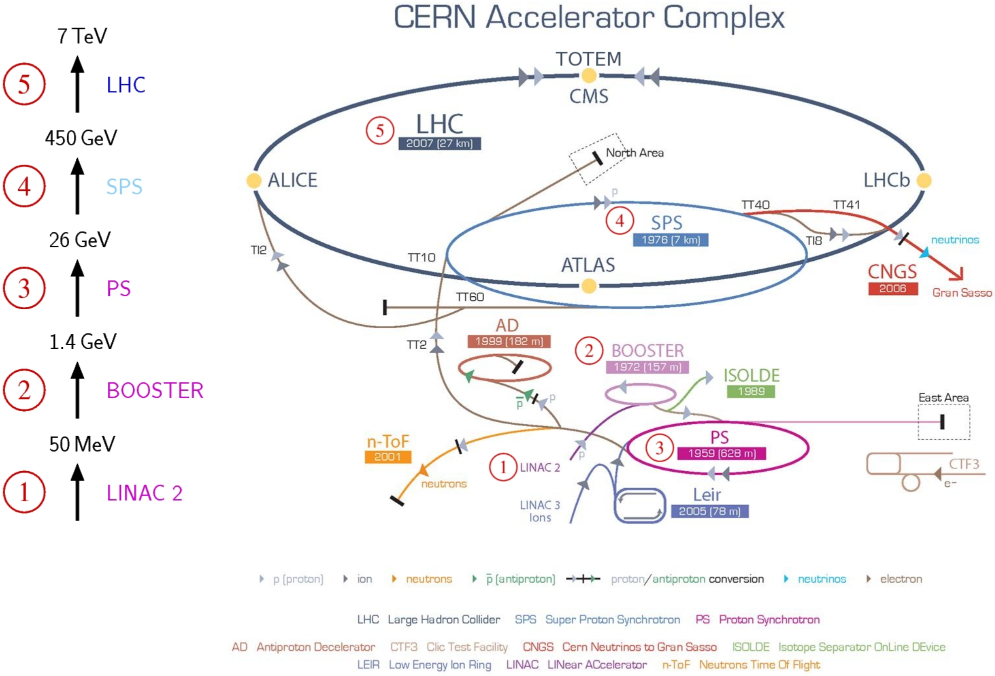

Figure 4: The CERN accelerator complex (right) and acceleration steps with achieved energies for protons (left) [57, 58].

The *Large Hadron Collider* (LHC) located at the European Organization for Nuclear Research ("*Conseil Européen pour la Recherche Nucléaire*" in short CERN) close to the French-Swiss border in the suburb of the Swiss city Geneva, is the world's largest particle collider. At 100 meters beneath the ground lies the main storage ring of the synchrotron type accelerator with a circumference of 27 kilometers. It consists of 8 radiofrequency cavities per beam, which accelerate the particles and 9300 superconducting magnets operated at 1.9 K, which produce a maximum magnetic field of 8.33 T and guide the particles through the vacuum tube. The LHC can currently (after the 2015 upgrade) achieve proton-proton (p-p) collisions with center of mass energies of up to $\sqrt{s_{NN}} = 13\,\text{TeV}$ and lead-lead (Pb-Pb) collisions up to $\sqrt{s_{NN}} = 5.02\,\text{TeV}$ per nucleon pair, but is designed to go up to 14 TeV for p-p and 5.52 TeV per nucleon pair[9] (or 1150 TeV total) for Pb-Pb. Per design, the protons inside the LHC are grouped into bunches of $1.1 \cdot 10^{11}$ ($7 \cdot 10^{7}$ for Pb) particles and at full load 2808 (592 for Pb) bunches separated by 25 ns or equivalently 7 m in distance travel through the ring at 99.9999991% the speed of light, traversing it 11 245 times per second. Although the beam on the collision points are collimated to 16 μm, when two proton bunches cross each other only 20 collision occur on average, but since these crossings happen with a frequency of $2808 \cdot 11\,245 = 31.6\,\text{MHz}$ this results in $20 \cdot 31.6\,\text{MHz} \approx 600$ million p-p collisions per second. Besides p-p and Pb-Pb collisions the LHC was also operated with p-Pb at $\sqrt{s_{NN}} = 5.02\,\text{TeV}$ and for the future also collisions of lighter ions than lead are foreseen.

---

[9] Out of 208 lead nucleons only 82 are charged protons, which can be accelerated by the fields, thus resulting in $82/208 \cdot 14\,\text{TeV} = 5.52\,\text{TeV}$.

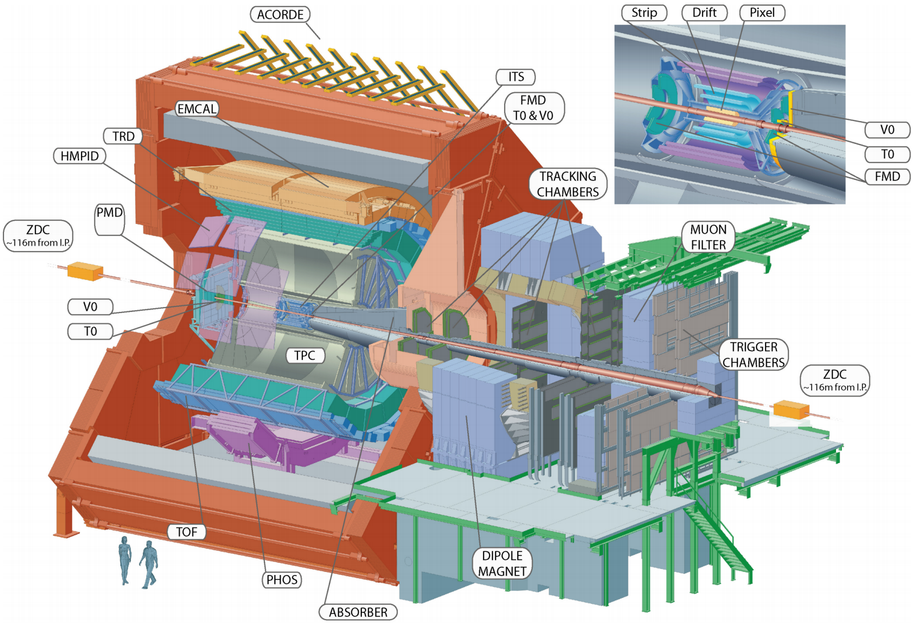

Figure 5: The ALICE experiment. The inner detectors are magnified and shown in the top right corner. [62]

The Pb-Pb collisions analyzed in this thesis are provided by the LHC, however, it needs a system of pre-accelerators (see Fig. 4) to bring the particles to relativistic speeds. Starting from a source of vaporized lead, the ions get initially accelerated by the linear accelerator Linac 3, from where they enter the *Low Energy Ion Ring* (LEIR), followed by the *Proton Synchrotron* (PS) and the *Super Proton Synchrotron* (SPS) before being finally ejected into the LHC.

Around the LHC ring are four main experiments located, namely: *A Large Ion Collider Experiment* (ALICE), *A Toroidal LHC ApparatuS* (ATLAS), *Compact Muon Solenoid* (CMS) and *Large Hadron Collider beauty* (LHCb). While ATLAS and CMS are general purpose experiments optimized for discovering new particles like the Higgs, LHCb is focused on bottom-quark physics in the forward regions. ALICE, from which the data of this thesis stem, is a dedicated heavy-ion experiment and is discussed in the following section.

In summary[10], the LHC brings together over 10 000 scientists and engineers from more than 100 countries, uses 1000 GWh energy and produces 15 PB of data per year.

2.2 A Large Ion Collider Experiment (ALICE)

ALICE is an experiment optimized for the study of strongly interacting QCD matter created in relativistic heavy-ion collisions[11]. In particular its main goal is to investigate the properties of the quark-gluon plasma. The experiment is optimized to provide high-momentum resolution as well as very good particle identification (PID) of the reconstructed tracks over a broad range of momentum while at the same time coping with the extreme particle multiplicities occurring in Pb-Pb collisions. The experiment with its dimensions of $16 \times 16 \times 26\,\mathrm{m}^3$ and a weight of about 10 000 t consists of 18 different detector systems. Starting at the center first comes the barrel containing the *Inner Tracking System* (ITS) of six layers of high-resolution *Silicon Pixel Detectors* (SPD), *Silicon Drift Detectors* (SDD)

---

[10] The facts presented in this section stem from [59–61]

[11] This section is based on [62–66].

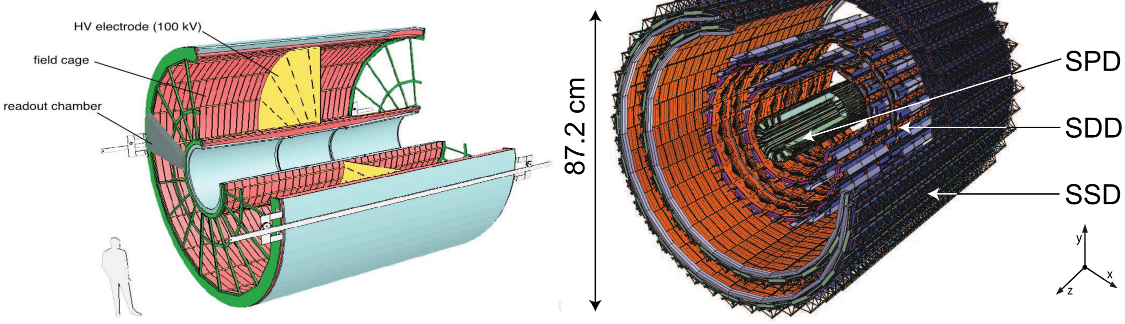

(a) (b)

Figure 6: The ALICE **a)** Time Projection Chamber [61] and **b)** Inner Tracking System [67].

and *Silicon Strip Detectors* (SSD), outside the barrel follows a cylindrical *Time Projection Chamber* (TPC) and three particle identification arrays consisting of *Time-of-Flight* (TOF), Ring Imaging Cherenkov (*High Momentum Particle Identification* - HMPID) and *Transition Radiation Detectors* (TRD), further followed by two *Electromagnetic Calorimeters* (PHOton Spectrometer - PHOS and EMCal).

The ITS is placed directly around the beam pipe and is used to determine the main interaction vertex as well as secondary vertices of fast decaying heavy flavor and strange particles. It can track low momentum particles, is used in PID, and has the highest spatial resolution among the ALICE detectors (which is needed so close to the beam axis). The primary tracking device is the cylindrical TPC positioned around the ITS. This gas filled apparatus covers the volume from inner radius $r = 85\,\text{cm}$ around the beam axis (minimal distance to distinguish tracks of different particles) to outer radius $r = 250\,\text{cm}$ (length required to get a good tracking and PID resolution). The TRD detector can be used to improve the momentum resolution at high momenta as well as to identify electrons. To further identify particles the TOF detector is used for charged hadrons and the HMPID for high momentum particles. To measure energy of charged particles and also to trigger on high p_T particles and improve jet measurements the EMCal can be used. What is left are photons and neutral mesons, which are identified in the PHOS. All the mentioned detectors are embedded in a solenoid magnet which creates a magnetic field of $B = 0.5\,\text{T}$.

So far detectors were discussed which are arranged perpendicular around the beam axis. However, ALICE also uses detectors in the forward and backward direction close to the beam pipe. A small *T0* detector located directly around the beam pipe, consisting of *Photo Multiplier Tubes* (PMT) acts as a trigger and longitudinal vertex position estimator and measures the event time. The *V0* detector provides minimum bias triggers and centrality triggers for the central barrel. To measure the charged particle multiplicity the *Forward Multiplicity Detector* (FMD) is used and for photon multiplicity the *Photon Multiplicity Detector* (PMD). At a distance of about 116 m away from the interaction region, but still close to the beam pipe, lie the *Zero Degree Calorimeters* (ZDC), which are important for the determination of the centrality by measuring spectator nucleons (see section 1.3.1). Lastly a forward muon spectrometer with 14 tracking and triggering chambers, a dipole magnet and an absorber can detect muon pairs from e.g. quarkonia decays.

2.2.1 Time Projection Chamber (TPC)

ALICE was designed with the goal of reconstructing all the individual tracks of the huge amount of particles produced in Pb-Pb collisions. Therefore a TPC was chosen as the primary tracking detector, since it can provide a fine track reconstruction due to a large amount of points for each track while still being fast enough[12] for the LHC Pb-Pb configuration which allows collisions at a rate of 10 MHz.

The TPC is a cylindrically shaped detector filled with $88\,\mathrm{m}^3$ of gas (90% Ne, 10% CO_2), which is separated by a cathode in the middle (see Fig. 6 a)) and has a size of 5 m along the beam axis and a radius up to 2.5 m. When a charged particle traverses the TPC gas volume it ionizes the gas atoms along its path. The liberated electrons then drift towards the end plates (which have a potential applied to them creating a uniform electric field) where they get registered by *Multi-Wire Proportional Chambers* (MWPC), which also amplify the primary electron signal. From the time an electron needs to reach the end plate a z coordinate of the causing particle can be reconstructed and the (r,φ) coordinates can directly be extracted from the MWPC, giving a full three dimensional track.

Concerning phase space coverage the TPC can detect particles in the transverse momentum range $0.1 < p_{\mathrm{T}} < 100\,\mathrm{GeV}/c$ with 6% resolution for $p_{\mathrm{T}} < 20\,\mathrm{GeV}/c$ in central Pb-Pb collisions [63]. The track finding efficiency saturates at about 90% for $p_{\mathrm{T}} > 1\,\mathrm{GeV}/c$ and the azimuthal resolution is about $\Delta\varphi = 0.7\,\mathrm{mrad}$ for the whole p_{T} range. Although the TPC covers full azimuth exception in the form of dead zones between the neighboring sectors (there are 16 sectors altogether) exist, essentially limiting the efficiency. Furthermore it has a pseudorapidity coverage of $|\eta| < 0.9$ for tracks traversing the whole radial length.

In addition to the TPC's main usage for tracking it can also be used for particle identification and centrality estimation [68]. To identify a particle the measured amplitude in the MWPC can be used for a dE/dx analysis combined with the particles momentum taken from the curvature of the path through the gas volume, which is inside a magnetic field.

Overall[13] the uniform azimuthal coverage of the TPC makes it the ideal detector for flow studies such as in this thesis, because non-uniform acceptance would result in systematic biases, which otherwise one has to correct for.

2.2.2 Inner Tracking System (ITS)

The ITS [60, 63, 67, 71] consists of 6 layers of silicon detectors using 3 different technologies. Its two innermost layers are composed of SPD, the next two of SDD and the last two of SSD. Being closest to the beam axis, the SPD has the highest spatial resolution. Both SPD layers together consist of 9.8×10^6 binary readout cells ($50 \times 70\,\mu\mathrm{m}$ in size), allowing them to separate two tracks for track densities of up to 80 tracks per cm^2. Arriving at the SSD the track density is less than $1\,\mathrm{cm}^{-2}$ and the spatial resolution of the sensor can be smaller. Combined the layers of the ITS can locate the primary vertex with a resolution better than $100\,\mu\mathrm{m}$. It can also give information about low p_{T} particles ($< 100\,\mathrm{MeV}/c$), which do not reach the TPC.

The ITS covers a pseudorapidity range of $|\eta| < 0.9$ for interaction vertices within 5 cm along the beam, although the first SPD layer has a coverage of $|\eta| < 2.0$.

Silicon itself is a semi-conductor and can be arranged in *pn-junctions*. By applying a voltage a depletion zone (depleted of thermal electrons) can be created, which is sensitive to

---

[12] However after the planned long shutdown 2 (LS2) in 2018 the luminosity of the LHC will be increased and the current readout method using Multi-Wire Proportional Chambers (MWPC) has to be upgraded to overcome the slowness resulting from a gating grid. It is planned to replace the MWPC with Gas Electron Multipliers (GEM) which offer continuous readout.

[13] This subsection used [60, 63, 69, 70].

particles. When a particle traverses a silicon sensor it excites the electrons in the material along its path into the valence band of the pn-junction, allowing them to drift to a readout interface. If the particle traversed all 6 layers a track can be fitted and charge and momentum of the particle can be found. Furthermore dE/dx analysis is possible in the 4 outer layers.

3 Anisotropic Flow

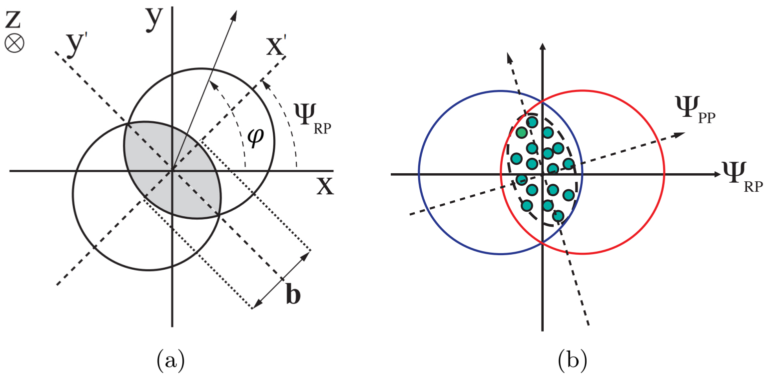

Figure 7: Schematic view of a non-central nucleus-nucleus collision drawn in the transverse plane perpendicular to the beam axis z showing in **a)** the reaction plane Ψ_{RP} and the impact parameter $|\mathbf{b}|$ [72] and in **b)** the difference between a reaction plane and the participant plane Ψ_{PP} [73, 74].

To constrain the properties of the QGP produced in ultrarelativistic heavy-ion collisions one studies azimuthal[14] anisotropies in the collective expansion of the produced system, which can only form if a strongly interacting medium is created and not if the collision of two nuclei is seen as a superposition of individual nucleon collisions. This collective expansion (described in section 1) is called flow [53]. Anisotropies in the flow develop due to an anisotropic overlap of the colliding nuclei (see Fig. 7 or Fig. 8) as well as to event-by-event fluctuating structures of the density profiles of the nuclei, leading to anisotropic pressure gradients in the hot and dense matter [75]. The pressure gradients therefore transform the initial spatial inhomogeneities and anisotropies into momentum anisotropies of the final state particles, which are experimentally accessible. The crucial hypothesis of pure flow phenomenon is that particles in a given event are emitted *independently* according to some azimuthal distribution. Since every azimuthal distribution is 2π periodic around the beam axis, it can be mathematically described by a Fourier series [76] which will be covered in the following section.

3.1 Flow Quantification

3.1.1 Geometric Description

Consider a non-central collision of two identical spherical nuclei, described by smooth Woods-Saxon nuclear density distributions, traveling in opposite directions (as can be seen in Fig. 4 a)). Anisotropic flow is characterized by the Fourier series description of the triple differential invariant distribution of emitted particles in an event with respect to the reaction plane, which can be written [76, 77] as

$$E\frac{d^3N}{d^3p} = \frac{d^3N}{p_\mathrm{T}\,dp_\mathrm{T}\,d\eta\,d\varphi} = \frac{1}{2\pi}\frac{d^2N}{p_\mathrm{T}\,dp_\mathrm{T}\,d\eta}\left(1 + 2\sum_{n=1}^{\infty} v_n(p_\mathrm{T},\eta)\cos[n(\varphi - \Psi_{RP})]\right) , \tag{4}$$

---

[14] Azimuthal directions are perpendicular to the beam axis. The azimuthal angle φ defines the direction of an emitted particle in the azimuthal plane (see Fig. 7).

where φ is the azimuthal angle of a particle, E the energy, p the total 3-momentum vector, p_T the transverse momentum, η the pseudorapidity and Ψ_{RP} is the angle defining the *reaction plane*, which is the plane spanned by the beam axis and the impact parameter vector (see Fig. 7 a))[15]. The description with respect to Ψ_{RP} is necessary, because in actual experiments the orientation of the impact parameter differs from event to event and Ψ_{RP} is therefore needed to compare quantities between different events. Sine terms in the series vanish due to reflection symmetry[16], leaving only even flow harmonics v_{2n} ($n \in \mathbb{N}$). Finally the Fourier coefficients v_n are called flow coefficients, in particular v_0 is called *radial flow*, v_1 *directed flow*, v_2 *elliptic flow*, v_3 *triangular flow* and so on, which are interpreted in the next section. The flow coefficients v_n can be expressed as

$$v_n(p_\mathrm{T},\eta) = \langle \cos\left[n(\varphi - \Psi_{RP}\right])\rangle = \frac{\int_0^{2\pi} \cos[n(\varphi-\Psi_{RP})] \frac{d^3N}{p_\mathrm{T}\, dp_\mathrm{T}\, d\eta\, d\varphi}\, d\varphi}{\int_0^{2\pi} \frac{d^3N}{p_\mathrm{T}\, dp_\mathrm{T}\, dy\, d\varphi}\, d\varphi} \tag{5}$$

(see Appendix A). They are in general p_T and η dependent and considering this dependence $v_n(p_\mathrm{T},\eta)$ is called n^th harmonic *differential flow* [73]. By averaging $v_n(p_\mathrm{T},\eta)$ over p_T and η with the invariant distribution as a weight[17] one gets the *integrated flow*.

To experimentally measure integrated flow, or more precisely flow coefficients, the all event average

$$\langle v_n(p_\mathrm{T},\eta)\rangle = \langle\langle \cos\left[n(\varphi - \Psi_{RP})\right]\rangle\rangle \tag{6}$$

is taken. For discrete measured particles $\langle\langle \ldots \rangle\rangle$ has to be read as: 1.) average over all particles in a chosen event and (p_T,η) bin and 2.) average over all events (in a centrality class). Integrated over transverse momentum and pseudorapidity in an all event averaged analysis, the particle distribution is therefore (as given in [53])

$$\frac{dN}{d\varphi} = \frac{\langle N\rangle}{2\pi}\left(1 + 2\sum_{n=1}^{\infty} \langle v_n(p_\mathrm{T},\eta)\rangle \cos[n(\varphi - \Psi_{RP})]\right) , \tag{7}$$

where $\langle N\rangle$ is the mean number of particles per event.

3.1.2 Event-by-Event Fluctuating Initial Geometry

In general the assumption used above of nuclei having smooth, spherical density distributions is not adequate, but rather one has to think of nuclei being made up of individual nucleon, or even more detailed, parton distributions (as can be seen in Fig. 8). These distributions can fluctuate event-by-event, breaking the picture of an “almond-shaped” collision region by creating an inhomogeneous energy density distribution. Only to leading order an elliptic shape of the collision region and its reflection symmetry are then given. Breaking reflection symmetry necessitates that the sine terms in the Fourier series (Eq. (4)) are not zero, which is equivalent to giving each term in the Fourier series an independent phase shift called *symmetry plane* Ψ_n instead of a global shift Ψ_{RP}. As a consequence odd flow harmonics v_{2n+1} ($n \in \mathbb{N}_0$) are non-vanishing due to such fluctuations. This conceptually changes[18]

---

[15] This plane is not directly measurable, but has to be estimated, for example with the event plane method [76] and is then called *event plane*.

[16] With the used assumptions “equal spherical nuclei and smooth distribution” it is equally probable to emit a particle in φ or in $-\varphi$ direction. Therefore $\sin(n\varphi) + \sin(n(-\varphi)) = \sin(n\varphi) - \sin(n\varphi) = 0$.

[17] For example over p_T: $v_n = \frac{\int_0^\infty v_n(p_\mathrm{T}) \frac{dN}{dp_\mathrm{T}} dp_\mathrm{T}}{\int_0^\infty \frac{dN}{dp_\mathrm{T}} dp_\mathrm{T}}$.

[18] But does not affect the experimental measurements, because both Ψ_n and Ψ_{RP} are not a priori known [78].

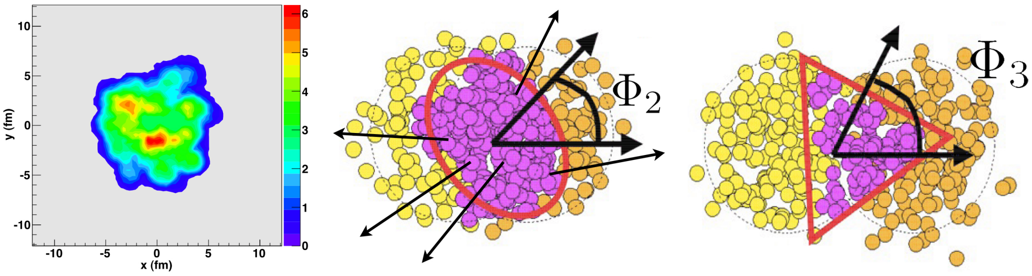

Figure 8: Left: Example initial state energy density distribution. Middle and Right: Example initial state symmetry planes Φ_2 and Φ_3 [80].

equations (4-7), which only hold for event-by-event fluctuating initial geometries if Ψ_{RP} is substituted by Ψ_n. For convenience:

$$E\frac{d^3N}{d^3p} = \frac{1}{2\pi}\frac{d^2N}{p_\mathrm{T}\,dp_\mathrm{T}\,d\eta}\left(1+2\sum_{n=1}^{\infty}v_n(p_\mathrm{T},\eta)\cos[n(\varphi-\Psi_n)]\right), \quad v_n(p_\mathrm{T},\eta) = \langle\cos[n(\varphi-\Psi_n)]\rangle\,, \tag{8}$$

$$\frac{dN}{d\varphi} = \frac{\langle N\rangle}{2\pi}\left(1+2\sum_{n=1}^{\infty}\langle v_n(p_\mathrm{T},\eta)\rangle\cos[n(\varphi-\langle\Psi_n\rangle)]\right), \quad \langle v_n(p_\mathrm{T},\eta)\rangle = \langle\langle\cos[n(\varphi-\langle\Psi_n\rangle)]\rangle\rangle\,. \tag{9}$$

Depending on the centrality of a collision one differentiates between a geometry-dominated regime in mid-central collisions and a fluctuation-dominated regime in the most central collisions [79]. The former one is characterized by the existence of the dominant harmonic v_2, which predominantly originates from the almond-shaped collision geometry in mid-central collisions. On the other hand, in the latter regime all harmonics can in principle be of comparable magnitude, since all of them solely stem from fluctuations.

For completeness, another commonly used global phase shift introduced for fluctuating initial geometries is the *participant plane* Ψ_{PP} defined by the dipole asymmetry of the initial energy density. This plane is not equal to Ψ_{RP} (see Fig. 7 b)) in general, but fluctuates around it. Therefore only in the absence of fluctuations these two planes coincide.

3.1.3 Initial Geometry and Final Momentum Distribution

As previously pointed out, anisotropic flow is generated by the initial anisotropy in the energy density of the colliding nuclei, which consists of the anisotropic overlap geometry and the fluctuations in the parton distributions, followed by an expansion of the produced medium. Flow is described by the coefficients v_n and the symmetry planes Ψ_n. In a similar way the initial coordinate space geometry can be described using eccentricities ϵ_n and symmetry plane angles Φ_n [78, 81–83]; in the center of mass system of the participating nucleons these degrees of freedom are given as

$$\epsilon_n = \frac{\sqrt{\langle r^n\cos(n\varphi)\rangle^2+\langle r^n\sin(n\varphi)\rangle^2}}{\langle r^n\rangle}, \quad n\Phi_n = \mathrm{atan2}\left(\langle r^n\sin(n\varphi)\rangle, \langle r^n\cos(n\varphi)\rangle\right)+\pi\,, \tag{10}$$

with (r,φ) the transverse position of the participating nucleons in polar coordinates [78, 83]. An important point to understand the system properties is how ϵ_n and Φ_n are related to v_n

and Ψ_n. Especially in early studies it was often assumed that v_n responds linearly to ϵ_n per harmonic n ($\epsilon_n \propto v_n$) and that $\Psi_n \simeq \Phi_n$ [78, 83–85]. However, more recent studies found that in general the dependence is non-linear and flow of harmonic n has contributions from different ϵ_n harmonics; furthermore $\Psi_n \neq \Phi_n$ [79, 86–88].

Although in experiments only the final state particles are physical observables and therefore the flow is measured and not the initial coordinate space distribution directly, different theoretical models try to describe directly the initial conditions. The most commonly used ones to simulate the initial energy and entropy density distribution are the *Monte Carlo Glauber* (MC Glauber) [54], the *Monte Carlo Kharzeev-Levin-Nardi Color Glass Condensate* (MC-KLN CGC) [89] and the *IP-Glasma* [49, 90–95] models.

In the Glauber MC model (see section 1.3.1) the event-by-event fluctuating distribution of nucleons is responsible for fluctuations of ϵ_n. In the MC-KLN model the energy density is calculated by the initial gluon production, which has spatial dependence and is obtained by a parametrization of the Color Glass Condensate model of gluon saturation in nuclei [96]. The IP-Glasma model in contrast to the two aforementioned ones also takes into account fluctuations of gluon fields inside the colliding nucleons and then evolves these using classical Yang-Mills dynamics, switching to hydrodynamic models after a matching surface (Cooper-Frye freeze-out surface [97]) [53].

4 Q-cumulants and Multiparticle Correlations

In the last section it was described how flow can be quantified and in theory also measured by equation (9) if the symmetry planes are experimentally accessible. Unfortunately the flow angles (i.e. the symmetry plane angles Ψ_n) are not directly measurable and new techniques have to be introduced to estimate flow harmonics v_n. The oldest and most frequently used method involves a direct estimation of Ψ_n via mean preferred directions of emitted particles and is commonly called *event plane method* (EP) [76, 98]. However, this method is biased by nonflow contributions. To improve the flow measurements methods based on cumulants, which are genuine multiparticle correlations, were developed and first mentioned in [99]. These methods systematically suppress nonflow effects. Since they would require construction of all possible particle multiplets an elegant formalism using the cumulant generating functions (GFC) was developed [99–101]. This approach still might lead to systematic biases, because it was derived using approximations (and hence will not be discussed in this thesis). The up to now final solution (that will also be used in all analyses presented in this thesis) lies in so called *Q-cumulants* (QC), which are cumulants, analytically expressed in terms of the moments of the flow vector. The following sections introduce this method and describe how it is used to estimate flow using *multiparticle correlations*, where the general argumentation of these sections is based on [53, 60, 61, 77, 99, 100, 102].

To complete this short overview, further methods besides the Q-cumulant method based on multiparticle correlations were developed, but will not be elaborated here. Most considerable are the *Lee-Yang zeros* (LYZ) method [103–106], which suppresses nonflow contributions to all orders and the *fitted q-distribution* (FQD) method, which fits a Bessel-Gaussian probability density function to an observable which is a function of the measured azimuthal angles (and hence has indirect sensitivity to v_n) but is per event invariant to Ψ_n [107].

4.1 Flow Vector Q_n

As a prerequisite for the following sections and as a central object in anisotropic flow analysis, the complex *flow vector*, or *Q-vector*, in harmonic n is generally introduced:

$$Q_n = |Q_n|\, e^{in\Psi'_n} \equiv \frac{1}{M}\sum_{j=1}^{M} e^{in\varphi_j} \,, \tag{11}$$

where M is the multiplicity of an event and φ_j the azimuthal angle of the j^{th} particle. It has to be noted that the prefactor $1/M$ might vary, further common definitions use $1/\sqrt{M}$ or just 1 (in later sections of this thesis it will for convenience reasons also chosen as 1). The reason for introducing this quantity is due to the cyclicity of the underlying problem; the 2π periodic flow analysis, and how to unfold it. One can depict the Q-vector for example in the following two ways: 1) One may think of a standard polar coordinate system. If the total interval $[0, 2\pi)$ is now divided into n equally sized subintervals (where each has its own 0 degree position), Q_n is measuring a mean value in each of the n subintervals followed by an average over all n mean values. Hence the angle is in the range $\Psi'_n \in [0, 2\pi/n)$. 2) One may neglect the $1/M$ prefactor and think of Q_n as being a random walk.

In other words Q_n can be seen as the n-periodic preferred direction of particle emission. This is also the original idea behind the event plane method, which assumes, that Ψ'_n is a good estimate of the corresponding Ψ_n in the underlying probability distribution (Eq. (8)).

4.2 Event Plane and Scalar Product Method

As the most intuitive approach the event plane method tries to estimate Ψ_n (the "true" symmetry plane from p.d.f. defined in Eq. (8)) by solving Eq. (11) for the phase[19]

$$\Psi'_n = \frac{1}{n}\arctan\left(\frac{\mathfrak{Im}\, Q_n}{\mathfrak{Re}\, Q_n}\right) = \frac{1}{n}\arctan\left(\frac{\sum_j \sin(n\varphi_j)}{\sum_j \cos(n\varphi_j)}\right) . \tag{12}$$

This formula can be improved by adding weights to correct for e.g. p_{T} or η efficiency:

$$\Psi'_n = \frac{1}{n}\arctan\left(\frac{\sum_j w_j \sin(n\varphi_j)}{\sum_j w_j \cos(n\varphi_j)}\right) . \tag{13}$$

It is important to note that only for an infinite number of particles per event $\Psi'_n \to \Psi_n$, therefore in experiments with limited number of particles there will always be an inaccuracy in determining Ψ_n, which via Eq. (9) lead to inaccuracies in the estimation of flow harmonics. To correct for this issue an *event plane resolution* R is introduced [98], which again cannot be measured directly but can be estimated by dividing the particle set into *sub-events* (with equal multiplicity) and then estimating Ψ'_n in each sub-event. In general the resolution is given [98, 108] by

$$R \equiv \left\langle e^{in(\Psi'_n - \Psi_n)} \right\rangle = \left\langle \frac{Q_n}{|Q_n|} e^{-in\Psi_n} \right\rangle = \left\langle \cos[n(\Psi'_n - \Psi_n)] \right\rangle , \tag{14}$$

where the last equality holds for reflection symmetry in absence of statistical fluctuations [108]. If split into two sub-events A and B with same multiplicity and resolution[20] each sub-event provides a symmetry plane estimate Ψ'^A_n, Ψ'^B_n via Eq. (12), out of which the resolution can be calculated [108, 109] as the correlation between these estimates:

$$R = \sqrt{\left\langle \frac{Q^A_n}{|Q^A_n|} \frac{Q^{B*}_n}{|Q^B_n|} \right\rangle} = \sqrt{\left\langle \cos[n(\Psi'^A_n - \Psi'^B_n)] \right\rangle} . \tag{15}$$

The final resolution corrected flow coefficients are then given by Eq. (9), where Ψ_n is estimated via Eq. (12), divided by the resolution in Eq. (15):

$$v_n\{EP\} = \frac{\left\langle Q_n \frac{Q^{A*}_n}{|Q^A_n|} \right\rangle}{\sqrt{\left\langle \frac{Q^A_n}{|Q^A_n|} \frac{Q^{B*}_n}{|Q^B_n|} \right\rangle}} . \tag{16}$$

Here Q_n is called a differential flow vector, because it is composed of particle of interest (POI), which can e.g. lie in a narrow p_{T}-, η-, etc. ranges, wheres $Q^{A(B)}_n$ come from sub-events $A(B)$ and can be chosen to contain many particles to improve statistical stability. Due to the fact that R calculated via Eq. (15) is always smaller than unity, the EP method always underestimates flow harmonics v_n, unless they are corrected for finite resolution.

---

[19] More exact, the atan2 function should be used, which computes the principal value of the argument function of a complex number to assure single-valuedness.

[20] E.g. by symmetric splitting around mid-rapidity and applying a gap in pseudorapidity.

At this point it is also worth mentioning another commonly used method, the *scalar product method*. Its simplest form is obtained by removing the absolute value factors $\left|Q_n^{A(B)}\right|$ in Eq. (16):

$$v_n\{SP\} = \frac{\left\langle Q_n \cdot Q_n^{A*} \right\rangle}{\sqrt{\left\langle Q_n^A \cdot Q_n^{B*} \right\rangle}} \,. \tag{17}$$

Compared to the event plane method, the scalar product method completely removes the explicit dependence on any symmetry plane (to see this compare the second and third term in Eq. (11)) – this can be seen as a preview for the following sections on multiparticle correlations.

However, the discussed methods do not come without flaws. In the era of precision flow measurements [108], especially the event plane method, although corrected for resolution, should be marked as deprecated. When it was developed the general assumption was that event-by-event flow fluctuations are negligible, i.e. flow is about constant per event. Since it is now known that they are not, it was investigated how they contribute to different methods [108, 110] with the result, that the event plane measurements are ambiguous due to detector acceptance and can give any value between the mean $\langle v_n \rangle$ (for infinite resolution) and the root-mean-square (RMS) $\sqrt{\langle v_n^2 \rangle}$ (for low resolution) [108]. This dependence on analysis details between different experiments makes it unfavorable to use this method since values can differ from a few percent for v_2, 10% for v_3 and higher harmonics up to a factor of 2 for mixed correlations (involving event planes from different harmonics) [108]. The scalar product method on the other hand, always yields the RMS [108].

In addition, methods based on multiparticle correlations also give clear estimates independent of acceptance but furthermore suppress nonflow. These will be the main topic of the subsequent sections.

4.3 Two- and Multiparticle Correlations

The problem in measuring flow coefficients directly via the simple equation (9) is due to Ψ_n not being a direct experimental observable. One could try to estimate Ψ_n as done with the event plane method or completely eliminate Ψ_n by using two- and *multiparticle azimuthal correlations*. The first idea of using particle pair correlations to measure collective flow was introduced in [111] and like the scalar product method (see Sec. 4.2) it only used 2-particle correlations. In the next sections a generalized formulation using (in theory) any amount of particles will be described. In order to achieve that the underlying objects called m-particle correlations (or correlators) are now introduced.

4.3.1 m-Particle Correlators

The most general *single-event* average m-particle correlation in harmonics $n_1, n_2, \ldots, n_m$ of particles with azimuthal angles $\varphi_{k_1}, \varphi_{k_2}, \ldots, \varphi_{k_m}$ is defined [102] as

$$\langle m \rangle_{n_1,n_2,\ldots,n_m} \equiv \left\langle e^{i(n_1\varphi_{k_1}+n_2\varphi_{k_2}+\cdots+n_m\varphi_{k_m})} \right\rangle \tag{18}$$

$$\equiv \frac{\displaystyle\sum_{\substack{k_1,k_2,\ldots,k_m=1\\(k_1\neq k_2\neq\cdots\neq k_m)}}^{M} w_{k_1}w_{k_2}\ldots w_{k_m} e^{i(n_1\varphi_{k_1}+n_2\varphi_{k_2}+\cdots+n_m\varphi_{k_m})}}{\displaystyle\sum_{\substack{k_1,k_2,\ldots,k_m=1\\(k_1\neq k_2\neq\cdots\neq k_m)}}^{M} w_{k_1}w_{k_2}\ldots w_{k_m}} \tag{19}$$

where M is again the multiplicity of an event and $w_{k_1}, w_{k_2}, \ldots, w_{k_m}$ are particle weights, which can be used to remove systematic biases originating from various detector inefficiencies[21]. It is emphasized that the condition $k_1 \neq k_2 \neq \cdots \neq k_m$ is important to remove autocorrelations, i.e. correlations from particles to itself (also called self-correlations), which can give a strong bias for particular combinations of harmonics[22]. For the typical flow analysis of single flow coefficients v_n only specific combinations of the free parameters are needed[23], which simplify this expression drastically. In particular only correlators of the form m even and $n_1 = n_2 = \cdots = -n_k - 1 = -n_k$ are needed where the sign of the harmonics changes at half (the subscripts, being redundant, will be suppressed; e.g. for 2-particle correlation $\langle 2\rangle_{n,-n} \equiv \langle 2\rangle$). Furthermore particle weights in this thesis are chosen to be unit, this will be justified in section 5.1 . Using these conditions the single-event average 2- and 4-particle azimuthal correlations read

$$\langle 2\rangle \equiv \left\langle e^{in(\varphi_1-\varphi_2)} \right\rangle \equiv \frac{1}{\binom{M}{2}2!} \sum_{\substack{i,j=1\\i\neq j}}^{M} e^{in(\varphi_i-\varphi_j)}\,, \tag{20}$$

$$\langle 4\rangle \equiv \left\langle e^{in(\varphi_1+\varphi_2-\varphi_3-\varphi_4)} \right\rangle \equiv \frac{1}{\binom{M}{4}4!} \sum_{\substack{i,j,k,l=1\\i\neq j\neq k\neq l}}^{M} e^{in(\varphi_i+\varphi_j-\varphi_k-\varphi_l)}\,. \tag{21}$$

In a second step the *all-event* average is defined as

$$\langle\langle 2\rangle\rangle \equiv \left\langle\left\langle e^{in(\varphi_1-\varphi_2)} \right\rangle\right\rangle \equiv \frac{\sum_{i=1}^{N}(w_{\langle 2\rangle})_i \langle 2\rangle_i}{\sum_{i=1}^{N}(w_{\langle 2\rangle})_i}\,, \tag{22}$$

$$\langle\langle 4\rangle\rangle \equiv \left\langle\left\langle e^{in(\varphi_1+\varphi_2-\varphi_3-\varphi_4)} \right\rangle\right\rangle \equiv \frac{\sum_{i=1}^{N}(w_{\langle 4\rangle})_i \langle 4\rangle_i}{\sum_{i=1}^{N}(w_{\langle 4\rangle})_i}\,, \tag{23}$$

---

[21] Typical weights might be φ-weights from non-uniform azimuthal acceptance, p_{T}-weights from non-uniform momentum reconstruction efficiency, etc. In general $w = w(\varphi, p_{\mathrm{T}}, \eta, \mathrm{PID}, \ldots)$.

[22] E.g. for isotropic harmonics satisfying $\sum_i n_i = 0$ self-correlations would give a trivial, non-negligible contribution of $e^0 = 1$.

[23] However, recently a generic framework to calculate these general correlators in an efficient recursive way was developed [102].

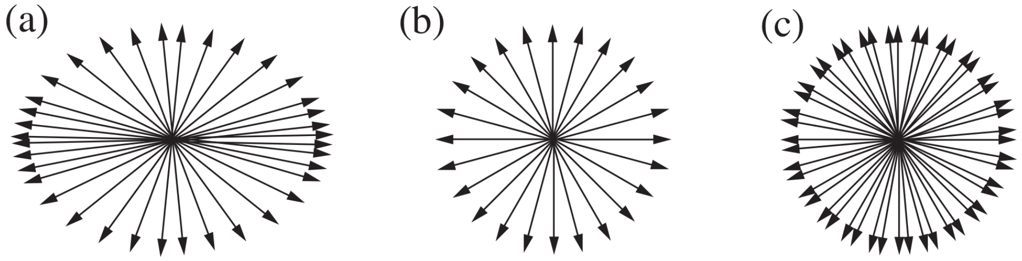

Figure 9: Azimuthal particle distributions, where **a)** $v_2 > 0$, $v_2\{2\} > 0$, **b)** $v_2 = 0$, $v_2\{2\} = 0$, **c)** $v_2 = 0$, $v_2\{2\} > 0$ [74].

where N is the number of events and $w_{\langle 2\rangle}, w_{\langle 4\rangle}$ are event weights, which are not arbitrary but since multiplicity fluctuates event-by-event have to be chosen[24] as the number of distinct m-particle combinations one can form for an event with multiplicity M [60]

$$w_{\langle m\rangle} \equiv \binom{M}{m} m!\,. \tag{24}$$

For 2- and 4-particle correlations they are respectively

$$w_{\langle 2\rangle} \equiv M(M-1)\,, \tag{25}$$
$$w_{\langle 4\rangle} \equiv M(M-1)(M-2)(M-3)\,. \tag{26}$$

4.4 Collective Flow and Nonflow

In flow analysis one in general differentiates between two kinds of correlations. On the one hand there is the concept of “collectivity” and on the other hand correlations between only a (small) subset of the produced particles. The former being the one flow analysis is interested in, the latter one, resulting from various kind of physical processes like momentum conservation, Bose-Einstein correlations, final state Coulomb interactions, jet fragmentation, resonance decays, etc., polluting the flow signal and thus labeled *nonflow*. When only collective anisotropic flow is present all produced particles are emitted *independently* to each other and are only correlated to some common symmetry plane. As a consequence the multivariate probability density function of m particles factorizes into the product of the normalized marginalized p.d.f. of each particle which are respectively given by the Fourier series in (7):

$$f(\varphi_1, \varphi_2, \dots, \varphi_m) = f_{\varphi_1}(\varphi_1) f_{\varphi_2}(\varphi_2) \cdots f_{\varphi_m}(\varphi_m)\,. \tag{27}$$

Furthermore, since collective anisotropic flow is a genuine multiparticle phenomenon, while nonflow typically involves only particles from a subset, genuine multiparticle correlations can be used to reduce the relative contributions from nonflow and to give a statement on whether v_n is dominated by flow or nonflow (see also section 4.6.6).

Figure 9 illustrates collective and non-collective effects exemplified by elliptic flow v_2. The left figure shows an anisotropic distribution yielding a value in elliptic flow greater than zero for both, the true value and the estimate using 2-particle correlations (indicated by the notation $\{2\}$). The middle figure depicts no elliptic flow and also no particle correlations leading to a value of zero. Figure 9 c) shows the difficulties originating from nonflow,

---

[24] In practice all measured correlations will be biased by nonflow contributions and one could tune the weights to reduce systematic bias. Unfortunately this is not possible in a consistent way, but could be done based on Monte Carlo event generation.

although there is no collective anisotropic flow, 2-particle correlations are present, which are clearly not due to the collective origin, but in this case due to a simple rotation of a duplicate of the initial distribution (in physical terms this reasoning could e.g. originate from resonance decays, where a particle track splits into two highly correlated new tracks).

4.5 Correlations and Flow

In the previous sections multiparticle correlations as well as collective anisotropic flow and factorization of the underlying p.d.f. were introduced. Both concepts can be combined to get a first estimate for the flow coefficients v_n:

$$\langle\langle 2\rangle\rangle \equiv \left\langle\left\langle e^{in(\varphi_1-\varphi_2)}\right\rangle\right\rangle = \left\langle\left\langle e^{in(\varphi_1-\Psi_n-(\varphi_2-\Psi_n))}\right\rangle\right\rangle \tag{28}$$

$$= \left\langle\left\langle e^{in(\varphi_1-\Psi_n)}\right\rangle \left\langle e^{-in(\varphi_2-\Psi_n)}\right\rangle + \delta_{2,n}\right\rangle \tag{29}$$

$$= \left\langle v_n^2 + \delta_{2,n}\right\rangle \tag{30}$$

$$\overset{\text{(flow)}}{=} \left\langle v_n^2\right\rangle , \tag{31}$$

$$\langle\langle 4\rangle\rangle \equiv \left\langle\left\langle e^{in(\varphi_1+\varphi_2-\varphi_3-\varphi_4)}\right\rangle\right\rangle = \left\langle\left\langle e^{in((\varphi_1-\Psi_n)+(\varphi_2-\Psi_n)-(\varphi_3-\Psi_n)-(\varphi_4-\Psi_n))}\right\rangle\right\rangle \tag{32}$$

$$= \left\langle v_n^4 + \delta_{4,n} + 4v_n^2\delta_{2,n} + 2\delta_{2,n}^2\right\rangle \tag{33}$$

$$\overset{\text{(flow)}}{=} \left\langle v_n^4\right\rangle . \tag{34}$$

Here the correlations were expanded[25] into a common correlation of each particle with the symmetry plane (which can be identified as v_n, see Eq. (9)) and correlations independent of the symmetry plane between the particles. The correlated terms are noted by $\delta_{m,n}$ for an m-particle correlation in harmonic n and are precisely the nonflow stated in the previous section. It can be also easily seen that for pure collective behavior and in the absence of nonflow the $\delta_{m,n}$ terms vanish and such a multiparticle correlator can be used to measure flow coefficients. This is also true for higher orders [60]

$$\langle\langle 6\rangle\rangle = \left\langle v_n^6\right\rangle , \quad \langle\langle 8\rangle\rangle = \left\langle v_n^8\right\rangle , \quad \dots . \tag{35}$$

4.6 Cumulants

The last section showed a decomposition of the 2- and 4-particle distributions (Eqs. (30) and (33)) because in general a complete factorization as in Eq. (27) breaks down due to nonflow effects. However, this decomposition can be explained in a rigorous mathematical sense using cumulant expansion. This section first introduces cumulants, shows how they are applied to multiparticle correlations and then connected to flow measurements. Furthermore an analytic way of describing cumulants in terms of Q-vectors, which is a breakthrough concerning computation time, is shown and deviations from ideal flow conditions, e.g. presence of flow fluctuations and nonflow, are discussed.

---

[25] The expansion, especially for 4-particle and higher correlations, is not too obvious and originates in the cumulant expansion, which is described in the next section.

4.6.1 Mathematical Formalism

Cumulants κ_r can be used to describe uni- or multivariate probability distributions and are an alternative to the moments of a distribution in a sense that for two p.d.f. whose moments are identical also the cumulants will be and vice versa. Since for flow analysis joined (or multivariate) cumulants are the important ones only a quick introduction to univariate cumulants is given.

4.6.1.1 Univariate Cumulants

Remembering the definitions of the moment of order $r \in \mathbb{N}_0$ of a real-valued random variable X with p.d.f. f

$$\mu_r \equiv E(X^r) \equiv \langle X^r \rangle \equiv \int_{-\infty}^{\infty} x^r f(x)\, dx, \tag{36}$$

and the moment *generating function* (MGF)

$$M(\xi) \equiv E(e^{\xi X}) = E\left(\sum_{r=0}^{\infty} \frac{(\xi X)^r}{r!}\right) = \sum_{r=0}^{\infty} \frac{\xi^r}{r!} E(X^r) = \sum_{r=0}^{\infty} \frac{\xi^r}{r!} \mu_r \,, \tag{37}$$

the *cumulant generating function* (CGF) is given [112] by taking the logarithm

$$K(\xi) = \log M(\xi) = \log E(e^{\xi X}) = \sum_r \frac{\xi^r}{r!} \kappa_r \,. \tag{38}$$

Both generating functions respectively combine all moments/cumulants in one expression out of which the moments/cumulants can in return be “generated” by taking the r^{th} derivative at the origin

$$\mu_r = M^{(r)}(0) = \left.\frac{\mathrm{d}^r M(\xi)}{\mathrm{d}\xi^r}\right|_{\xi=0}, \quad \kappa_r = K^{(r)}(0) = \left.\frac{\mathrm{d}^r K(\xi)}{\mathrm{d}\xi^r}\right|_{\xi=0}. \tag{39}$$

As mentioned, moments can be expressed in terms of cumulants and vice versa, using Faà di Bruno’s formula for higher derivatives of composite functions the analytic expressions read [113]

$$\mu_r = \sum_{k=1}^{r} B_{r,k}(\kappa_1, \ldots, \kappa_{r-k+1}) \,, \quad \kappa_r = \sum_{k=1}^{r} (-1)^{k-1}(k-1)! B_{r,k}(\mu_1, \ldots, \mu_{r-k+1}) \,, \tag{40}$$

where $B_{r,k}$ are the partial or incomplete exponential Bell polynomials. In particular the first few relations are

$$\mu_1 = \kappa_1 \qquad \kappa_1 = \mu_1 \tag{41}$$

$$\mu_2 = \kappa_2 + \kappa_1^2 \qquad \kappa_2 = \mu_2 - {\mu_1}^2 \tag{42}$$

$$\mu_3 = \kappa_3 + 3\kappa_2\kappa_1 + \kappa_1^3 \qquad \kappa_3 = \mu_3 - 3\mu_2\mu_1 + 2{\mu_1}^3 \tag{43}$$

$$\mu_4 = \kappa_4 + 4\kappa_3\kappa_1 + 3\kappa_2^2 + 6\kappa_2\kappa_1^2 + \kappa_1^4 \qquad \kappa_4 = \mu_4 - 4\mu_3\mu_1 - 3{\mu_2}^2 + 12\mu_2{\mu_1}^2 - 6{\mu_1}^4 \tag{44}$$

and it can be seen that to express the r^{th} moment(cumulant) the first r cumulants(moments) are needed. Furthermore a recursion exists which relates cumulants and moments

$$\kappa_r = \mu_r - \sum_{m=1}^{r-1} \binom{r-1}{m-1} \kappa_m \mu_{r-m} \,. \tag{45}$$

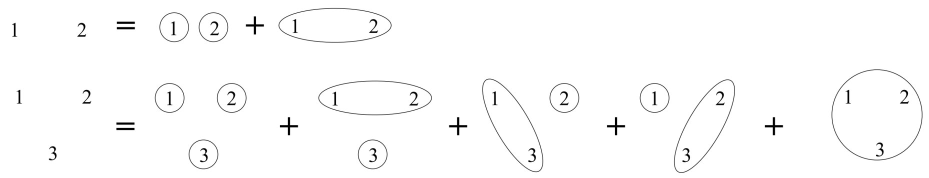

Figure 10: Partition of a 2- and 3-element set into non-empty subsets [99].

Lastly moments expressed in terms of cumulants have a strong link to combinatorics, as will be further discussed in 4.6.2. In particular they describe partition of sets. A partition of a set is a grouping of the set's elements into non-empty subsets (called blocks) in a way that every element is included in one (and only one) of the subsets. This property using cumulants becomes more easy to see if the r^{th} moment is written as [114]

$$\mu_r = E(X^r) = \sum_{\pi} \prod_{B\in\pi} \kappa_{|B|} \tag{46}$$

where π iterates through all possible partitions of a set of size r, B is one of the blocks into which the set is partitioned and $|B|$ is the size of the block. Therefore each term in the sum is a product of cumulants whose indices add up to r.

4.6.1.2 Multivariate Cumulants - Joined Cumulants

For a set of m random variables $S = \{X_1, X_2, \ldots, X_m\}$ the CGF straightforwardly generalizes to

$$K(\xi_1, \xi_2, \ldots, \xi_m) = \log E\left(e^{\sum_{j=1}^{m} \xi_j X_j}\right) . \tag{47}$$

As an analytic expression [115, 116] the joined cumulants read

$$\kappa(X_1, \ldots, X_m) = \sum_{\pi} (|\pi| - 1)!(-1)^{|\pi|-1} \prod_{B\in\pi} E\left(\prod_{i\in B} X_i\right) , \tag{48}$$

where π iterates over the set of all possible partitions, B runs through all blocks of partition π and $|\pi|$ is the number of blocks in partition π. Also Eq. (46) can be generalized:

$$E(X_1 \cdots X_m) = \sum_{\pi} \prod_{B\in\pi} \kappa(X_i : i \in B) . \tag{49}$$

An interesting connection occurs when the random variables $X_1, X_2, \ldots, X_m$ become indistinguishable and the corresponding joined cumulant "collapses" into the m^{th} univariate analogon: $\kappa(S) = \kappa(\underbrace{X, X, \ldots, X}_{m\,\text{times}}) = \kappa_m(X) \equiv \kappa_m$. Moreover a joined cumulant of 2 variables is exactly the covariance $\kappa(X_1, X_2) = \text{cov}(X_1, X_2)$ and combined with the aforementioned collapse when the variables become indistinguishable, this gives the variance $\kappa(X, X) = \text{cov}(X, X) = \text{var}(X)$. Also trivially $\kappa(X_1) = \kappa_1 = E(X_1)$.

To disentangle especially Eqs. (49) and (48), some examples are now given and depicted. The easier to depict equation is (49). Starting with the trivial case

- $\mathbf{m = 1}$: There is exactly one partition π_1 into non-empty sub-sets of a set $S = \{X_1\}$ with one element, namely the set itself. The first (and only) partition π_1 has therefore only one block $B_{1,1}$ of size $\left|B_{1,1}\right| = 1$ and in total this yields

$$E(X_1) = \kappa(X_1) . \tag{50}$$

- **m = 2** : Going a step further to $m = 2$ random variables there are two different partitions, which are also visualized in the top of Fig. 10,

$$\pi_1 = \{B_{1,1}, B_{1,2}\} = \{\{X_1\}, \{X_2\}\}\,, \tag{51}$$

$$\pi_2 = \{B_{2,1}\} \qquad = \{\{X_1, X_2\}\}\,. \tag{52}$$

The first possible partition π_1 consists of two blocks $B_{1,1}, B_{1,2}$ with one element each. The second partition π_2 consists of only one block $B_{2,1}$ but with two elements. Combined this gives

$$E(X_1X_2) = \kappa(X_1)\kappa(X_2) + \kappa(X_1, X_2) \tag{53}$$

$$= E(X_1)E(X_2) + \kappa(X_1, X_2)\,. \tag{54}$$

where in the last step Eq. (50) was used.

- **m = 3** : For three random variables the possible partitions into non-empty sub-subsets (also illustrated in Fig. 10 bottom) are

$$\pi_1 = \{B_{1,1}, B_{1,2}, B_{1,3}\} = \{\{X_1\}, \{X_2\}, \{X_3\}\}\,, \tag{55}$$

$$\pi_2 = \{B_{2,1}, B_{2,2}\} \qquad = \{\{X_1, X_2\}, \{X_3\}\}\,, \tag{56}$$

$$\pi_3 = \{B_{3,1}, B_{3,2}\} \qquad = \{\{X_1, X_3\}, \{X_2\}\}\,, \tag{57}$$

$$\pi_4 = \{B_{4,1}, B_{4,2}\} \qquad = \{\{X_2, X_3\}, \{X_1\}\}\,, \tag{58}$$

$$\pi_5 = \{B_{5,1}\} \qquad = \{\{X_2, X_3, X_1\}\}\,. \tag{59}$$

Thus the whole sum reads

$$\begin{aligned} E(X_1X_2X_3) =& \kappa(X_1)\kappa(X_2)\kappa(X_3) \\ &+ \kappa(X_1, X_2)\kappa(X_3) + \kappa(X_1, X_3)\kappa(X_2) + \kappa(X_2, X_3)\kappa(X_1) \qquad (60) \\ &+ \kappa(X_1, X_2, X_3) \\ =& E(X_1)E(X_2)E(X_3) \\ &+ \kappa(X_1, X_2)E(X_3) + \kappa(X_1, X_3)E(X_2) + \kappa(X_2, X_3)E(X_1) \qquad (61) \\ &+ \kappa(X_1, X_2, X_3) \\ =& E(X_1)E(X_2)E(X_3) \\ &+ \left[E(X_1X_2) - E(X_1)E(X_2)\right] E(X_3) \\ &+ \left[E(X_1X_3) - E(X_1)E(X_3)\right] E(X_2) \qquad (62) \\ &+ \left[E(X_2X_3) - E(X_2)E(X_3)\right] E(X_1) \\ &+ \kappa(X_1, X_2, X_3) \\ =& -2E(X_1)E(X_2)E(X_3) \\ &+ E(X_1X_2)E(X_3) + E(X_1X_3)E(X_2) + E(X_2X_3)E(X_1) \qquad (63) \\ &+ \kappa(X_1, X_2, X_3)\,, \end{aligned}$$

where in the first step from Eq. (60) to (61) equation (50) was inserted and in the second step from Eq. (61) to (62) equation (54) was used.

In this example the recursive nature of the underlying problem can be seen. For each newly added random variable a new cumulant arises of the order of random variables in the expectation value. To express the expectation value of a product of m random variables solely in terms of lower number of random variables expectation values is possible up to the m variable joint cumulant. Or argued the other way around:

The m random variable cumulant can be purely expressed as a combination of expectation values of m and less random variables (which is exactly what Eq. (48) says).

Either by looking at Eq. (48) or by solving Eq. (54) and (63) for their respective cumulant one gets

$$\kappa(X_1, X_2) = E(X_1 X_2) - E(X_1)E(X_2)\,, \tag{64}$$

$$\begin{aligned}\kappa(X_1, X_2, X_3) = &E(X_1 X_2 X_3) \\ &- E(X_1X_2)E(X_3) - E(X_1X_3)E(X_2) - E(X_2X_3)E(X_1) \\ &+ 2E(X_1)E(X_2)E(X_3)\,.\end{aligned} \tag{65}$$

Since Eq. (49) is now understood it is easy to see that Eq. (48) is basically the same just with $E(\dots)$ interchanged with $\kappa(\dots)$ and a weighting factor for each term depending on the block size $|\pi|$.

At the end of this mathematical overview of cumulants a possible interpretation of the meaning of cumulants is given. From the previous example it can be seen that the joint cumulant acts as a measure of how far random variables are from independence, completely vanishing for independence. This is easily realized by looking at the cumulant expressed solely by expectation values, because for independent variables the expectation value factorizes and hence all terms cancel. Or in other words

The joined cumulant of m random variables $X_1, \dots, X_m$ measures the interaction of the variables which is *genuinely* of m-body type (where interaction means the opposite of independence).

4.6.2 Cumulant Expansion of Multiparticle Correlations

In section 4.6.1 the objects of interest were mainly the expectation values and the cumulants. However the objects of interest in this thesis are multiparticle correlations. Fortunately the framework of cumulants can easily be applied to multiparticle correlations. In particular for a given m particle correlator

$$\langle m\rangle = \left\langle e^{in(\varphi_1+\varphi_2+\dots-\varphi_{m-1}-\varphi_m)}\right\rangle = \left\langle e^{in\varphi_1}e^{in\varphi_2}\cdots e^{-in\varphi_{m-1}}e^{-in\varphi_m}\right\rangle \tag{66}$$

the event-average $\langle\dots\rangle$ equates to the expectation value $E(\dots)$ and the individual factorized exponential functions can be identified as the random variables with the following mathematical description:

$$X_1 \equiv e^{in\varphi_1}, \quad X_2 \equiv e^{in\varphi_2}, \quad \dots \quad , \quad X_{m-1} \equiv e^{in\varphi_{m-1}}, \quad X_m \equiv e^{in\varphi_m}\,. \tag{67}$$

In practice the cumulant cannot be measured directly, but since it can be expressed in terms of expectation values it can be obtained indirectly. Unfortunately, looking at the definition of the expectation value (e.g. in Eq. (36)) a problem arises, namely the the needed joint multivariate p.d.f. is not know. Nevertheless, the all-event sample averages (see e.g. Eqs. (22), (23)) can be used as unbiased estimators for the expectation values. Therefore the multiparticle cumulants read

$$c_n\{1\} \equiv \langle\langle e^{in\varphi_1}\rangle\rangle\,, \tag{68}$$

$$c_n\{2\} \equiv \langle\langle e^{in(\varphi_1-\varphi_2)}\rangle\rangle - \langle\langle e^{in\varphi_1}\rangle\rangle\langle\langle e^{-in\varphi_2}\rangle\rangle\,, \tag{69}$$

$$\begin{aligned} c_n\{3\} \equiv\ & \langle\langle e^{in(\varphi_1+\varphi_2-\varphi_3)}\rangle\rangle \\ & - \langle\langle e^{in(\varphi_1+\varphi_2)}\rangle\rangle\langle\langle e^{-in\varphi_3}\rangle\rangle \\ & - \langle\langle e^{in(\varphi_1-\varphi_3)}\rangle\rangle\langle\langle e^{in\varphi_2}\rangle\rangle \\ & - \langle\langle e^{in(\varphi_2-\varphi_3)}\rangle\rangle\langle\langle e^{in\varphi_1}\rangle\rangle \\ & + 2\cdot\langle\langle e^{in\varphi_1}\rangle\rangle\langle\langle e^{in\varphi_2}\rangle\rangle\langle\langle e^{-in\varphi_3}\rangle\rangle\,, \end{aligned} \tag{70}$$

where the notation $c_n\{m\}$ means "cumulant estimated with m-particle correlations in harmonic n". There are two arguments which help simplifying these equations: 1) Objects like $\langle\langle e^{in(\varphi_1-\varphi_2)}\rangle\rangle$ and $\langle\langle e^{in(\varphi_1-\varphi_3)}\rangle\rangle$ are the same physical quantity, because the average is in both cases done over all two-particle combinations and hence they are just mathematical relabellings. 2) For detectors with uniform acceptance[26] only isotropic combinations of harmonics, i.e. $\sum_i n_i = 0$, yield non-zero multiparticle correlators after the all-event average (because the average is done in the laboratory frame and not with respect to a symmetry plane) and with all harmonics fixed as $n_i = n$ this translates that all odd particle number correlations like $\langle\langle e^{in\varphi_1}\rangle\rangle$ or $\langle\langle e^{in(\varphi_1+\varphi_2-\varphi_3)}\rangle\rangle$ will also vanish. The final unbiased estimators for the true cumulants for uniform acceptance are

$$c_n\{2\} = \langle\langle 2\rangle\rangle \tag{71}$$

$$c_n\{4\} = \langle\langle 4\rangle\rangle - 2\cdot\langle\langle 2\rangle\rangle^2\,, \tag{72}$$

$$c_n\{6\} = \big\langle\langle 6\rangle\big\rangle - 9\cdot\big\langle\langle 2\rangle\big\rangle\big\langle\langle 4\rangle\big\rangle + 12\cdot\big\langle\langle 2\rangle\big\rangle^3\,, \tag{73}$$

$$c_n\{8\} = \big\langle\langle 8\rangle\big\rangle - 16\cdot\big\langle\langle 6\rangle\big\rangle\big\langle\langle 2\rangle\big\rangle - 18\cdot\big\langle\langle 4\rangle\big\rangle^2 + 144\cdot\big\langle\langle 4\rangle\big\rangle\big\langle\langle 2\rangle\big\rangle^2 - 144\cdot\big\langle\langle 2\rangle\big\rangle^4\,, \tag{74}$$

and

$$c_n\{1\} = c_n\{3\} = c_n\{5\} = c_n\{7\} = \cdots = 0\,. \tag{75}$$

The higher order cumulants are added for completeness [60] and can be calculated in the same manner as it was discussed in the previous sections.

4.6.3 Cumulants and Flow

The step from multiparticle cumulants to an estimator for flow coefficients is straightforward. For example starting with the 2-particle cumulant Eq. (71) the 2-particle correlation can be rewritten as in Eq. (30) to get

$$\begin{aligned} c_n\{2\} &= \langle\langle 2\rangle\rangle && (76)\\ &= \left\langle v_n^2 + \delta_{2,n}\right\rangle && (77)\\ &= \left\langle v_n^2\right\rangle + \langle\delta_{2,n}\rangle && (78)\\ &\overset{\text{(flow)}}{=} \left\langle v_n^2\right\rangle\,, && (79) \end{aligned}$$

---

[26] For a discussion on non-uniform acceptance cumulants, where all terms have to be taken into account, see for example [60]. As mentioned before, the data used in this thesis is uniform.

where first the linearity of the expectation operator was used and in the last step nonflow was neglected. For the 4-particle cumulant in Eq. (72), the 2- and 4-particle correlations can be rewritten by Eqs. (30) and (33) to get

$$\begin{align}
c_n\{4\} &= \langle\langle 4\rangle\rangle - 2\cdot\langle\langle 2\rangle\rangle^2 \tag{80}\\
&= \left\langle v_n^4 + \delta_{4,n} + 4v_n^2\delta_{2,n} + 2\delta_{2,n}^2 \right\rangle - 2\left\langle v_n^2 + \delta_{2,n}\right\rangle^2 \tag{81}\\
&= \left\langle v_n^4\right\rangle + \left\langle \delta_{4,n}\right\rangle + 4\left\langle v_n^2\delta_{2,n}\right\rangle + 2\left\langle \delta_{2,n}^2\right\rangle - 2\left(\left\langle v_n^2\right\rangle + \left\langle \delta_{2,n}\right\rangle\right)^2 \tag{82}\\
&= \left\langle v_n^4\right\rangle + \left\langle \delta_{4,n}\right\rangle + 4\left\langle v_n^2\delta_{2,n}\right\rangle + 2\left\langle \delta_{2,n}^2\right\rangle - 2\left(\left\langle v_n^2\right\rangle^2 + 2\left\langle v_n^2\right\rangle\left\langle \delta_{2,n}\right\rangle + \left\langle \delta_{2,n}\right\rangle^2\right) \tag{83}\\
&= \left\langle -v_n^4\right\rangle + \left\langle \delta_{4,n}\right\rangle \tag{84}\\
&\overset{\text{(flow)}}{=} \left\langle -v_n^4\right\rangle , \tag{85}
\end{align}$$

where further assumption had to be made, namely $\langle\delta_{2,n}\rangle^2 = \langle\delta_{2,n}^2\rangle$ and $\langle v_n^2\rangle^2 = \langle v_n^4\rangle$ meaning event-by-event fluctuations in v_n and $\delta_{2,n}^2$ are negligible and $\langle v_n^2\delta_{2,n}\rangle = \langle v_n^2\rangle\langle\delta_{2,n}\rangle$ meaning flow and nonflow are not correlated. Again for completeness the higher order cumulants under the same assumptions respectively read

$$c_n\{6\} \overset{\text{(flow)}}{=} \left\langle 4v_n^6\right\rangle , \qquad c_n\{8\} \overset{\text{(flow)}}{=} \left\langle -33v_n^8\right\rangle . \tag{86}$$

It should be noted that an alternating pattern in the sign is visible, which can act as a necessary (not sufficient though) condition to estimate if flow of harmonic n is dominated by systematic bias or collective flow.

The reference flow estimates can then finally be obtained by canceling the prefactor and taking the corresponding root. In summary:

$$\begin{align}
v_n\{2\} &\equiv \sqrt{c_n\{2\}} = \sqrt{\langle\langle 2\rangle\rangle} = \sqrt{\langle v_n^2\rangle} \simeq \langle v_n\rangle , \tag{87}\\
v_n\{4\} &\equiv \sqrt[4]{-c_n\{4\}} = \sqrt[4]{-\left(\langle\langle 4\rangle\rangle - 2\cdot\langle\langle 2\rangle\rangle^2\right)} = \sqrt[4]{-\left(\langle v_n^4\rangle - 2\cdot\langle v_n^2\rangle^2\right)} \simeq \langle v_n\rangle , \tag{88}\\
v_n\{6\} &\equiv \sqrt[6]{\frac{1}{4}c_n\{6\}} = \sqrt[6]{\frac{1}{4}\left(\langle\langle 6\rangle\rangle - 9\cdot\langle\langle 2\rangle\rangle\langle\langle 4\rangle\rangle + 12\cdot\langle\langle 2\rangle\rangle^3\right)} \tag{89}\\
&= \sqrt[6]{\frac{1}{4}\left(\left\langle v_n^6\right\rangle - 9\cdot\left\langle v_n^2\right\rangle\left\langle v_n^4\right\rangle + 12\cdot\left\langle v_n^2\right\rangle^3\right)} \simeq \langle v_n\rangle , \tag{90}\\
v_n\{8\} &\equiv \sqrt[8]{-\frac{1}{33}c_n\{8\}} \tag{91}\\
&= \sqrt[8]{-\frac{1}{33}\left(\langle\langle 8\rangle\rangle - 16\cdot\langle\langle 6\rangle\rangle\langle\langle 2\rangle\rangle - 18\cdot\langle\langle 4\rangle\rangle^2 + 144\cdot\langle\langle 4\rangle\rangle\langle\langle 2\rangle\rangle^2 - 144\cdot\langle\langle 2\rangle\rangle^4\right)} \tag{92}\\
&= \sqrt[8]{-\frac{1}{33}\left(\left\langle v_n^8\right\rangle - 16\cdot\left\langle v_n^6\right\rangle\left\langle v_n^2\right\rangle - 18\cdot\left\langle v_n^4\right\rangle^2 + 144\cdot\left\langle v_n^4\right\rangle\left\langle v_n^2\right\rangle^2 - 144\cdot\left\langle v_n^2\right\rangle^4\right)} \tag{93}\\
&\simeq \langle v_n\rangle , \tag{94}
\end{align}$$

where $v_n\{m\}$ reads "reference flow coefficient v_n in harmonic n estimated with m-particle cumulant". All estimate the same flow harmonic v_n but are plagued by different systematic biases due to nonflow, statistical fluctuations, etc. and therefore the different notation is used.

4.6.4 Q-cumulants

During the last sections a sophisticated method for estimating flow with cumulants expressed in terms of multiparticle correlations, which is able to systematically suppresses unwanted effects of nonflow, was developed and is in principle ready to use in data analyses. Yet there is another point which can be improved, namely when it comes to implementing Eqs. (87) – (94) one is unavoidably confronted with implementing multiparticle correlators as e.g. in Eqs. (20) and (21). These correlators are averaged over all possible particle combinations (without autocorrelations) of one event, which equates in the numerical implementation to a brute-force approach of nested loops, in particular to evaluate an m-particle correlator m nested loops are needed. This corresponds to a complexity of $\mathcal{O}(M^m)$, which for LHC multiplicities going up to around $M \approx 2500$ is unfeasible to evaluate. The improved method avoiding this problem while still preserving the elimination of autocorrelations is called *Q-cumulants* (QC) method [77] and is based on flow vectors. For convenience the flow vector will now be reintroduced (and this definition is kept for the rest of the thesis) with a different prefactor to simplify the equations:

$$Q_n \equiv \sum_{j=1}^{M} e^{in\varphi_j} \,, \tag{95}$$

where again M is the number of particles in an event, φ_j are the azimuthal angles of the produced particles and n is the flow harmonic. The main idea of this method is to analytically express multiparticle correlations in terms of Q-vectors evaluated in different harmonics $n, 2n, 3n, \ldots$ and then use Eqs. (87) – (94) to estimate the flow coefficients.

For illustration the 2-particle Q-cumulant is derived in detail. Since the goal is to express Eq. (20) (which has per definition removed autocorrelations) with Q-vectors it is taken as a starting point and consecutively rearranged

$$\begin{aligned}
\langle 2 \rangle &= \frac{1}{\binom{M}{2} 2!} \sum_{\substack{i,j=1 \\ i \neq j}}^{M} e^{in(\varphi_i - \varphi_j)} = \frac{1}{M(M-1)} \sum_{\substack{i,j=1 \\ i \neq j}}^{M} e^{in(\varphi_i - \varphi_j)} && (96) \\
&= \frac{1}{M(M-1)} \left(\sum_{i,j=1}^{M} e^{in(\varphi_i - \varphi_j)} - \sum_{i=1}^{M} e^{in(\varphi_i - \varphi_i)} \right) && (97) \\
&= \frac{1}{M(M-1)} \left(\sum_{i=1}^{M} e^{in\varphi_i} \sum_{j=1}^{M} e^{-\varphi_j} - \sum_{i=1}^{M} 1 \right) && (98) \\
&= \frac{1}{M(M-1)} \left(Q_n Q_n^* - M \right) && (99) \\
&= \frac{|Q_n|^2 - M}{M(M-1)} \,, && (100)
\end{aligned}$$

where the crucial part was to expand the condition in the sum which removes autocorrelation. Using the same idea of expanding the initial interlaced sum (while preserving autocorrelation removal), which again can recursively be broken down to a level of plain Q-vectors, one gets [60] for higher orders (which quickly grow in number of terms, in fact the number of distinct terms per correlator form a Bell sequence [102], therefore the 8-particle correlator is omitted)

$$\langle 4 \rangle = \frac{|Q_n|^4 + |Q_{2n}|^2 - 2 \cdot \mathfrak{Re}\left[Q_{2n} Q_n^* Q_n^*\right]}{M(M-1)(M-2)(M-3)} - 2\,\frac{2(M-2) \cdot |Q_n|^2 - M(M-3)}{M(M-1)(M-2)(M-3)} \,, \tag{101}$$

$$\begin{aligned}
\langle 6 \rangle = & \frac{|Q_n|^6 + 9 \cdot |Q_{2n}|^2 \, |Q_n|^2 - 6 \cdot \mathfrak{Re}\left[Q_{2n} Q_n Q_n^* Q_n^* Q_n^*\right]}{M(M-1)(M-2)(M-3)(M-4)(M-5)} \\
& + 4\,\frac{\mathfrak{Re}\left[Q_{3n} Q_n^* Q_n^* Q_n^*\right] - 3 \cdot \mathfrak{Re}\left[Q_{3n} Q_{2n}^* Q_n^*\right]}{M(M-1)(M-2)(M-3)(M-4)(M-5)} \\
& + 2\,\frac{9(M-4) \cdot \mathfrak{Re}\left[Q_{2n} Q_n^* Q_n^*\right] + 2 \cdot |Q_{3n}|^2}{M(M-1)(M-2)(M-3)(M-4)(M-5)} \\
& - 9\,\frac{|Q_n|^4 + |Q_{2n}|^2}{M(M-1)(M-2)(M-3)(M-5)} \\
& + 18\,\frac{|Q_n|^2}{M(M-1)(M-3)(M-4)} \\
& - \frac{6}{(M-1)(M-2)(M-3)} \,.
\end{aligned} \tag{102}$$

In the final step the event averaged correlations $\langle\langle 2 \rangle\rangle$, $\langle\langle 4 \rangle\rangle$, ... can be obtained from Eqs. (22), (23), etc. and can then be inserted into Eqs. (87) – (94) to get the final flow estimate with Q-cumulants.

The important note here is that these Q-cumulant flow estimates (for uniform acceptance) can be evaluated in one run over the data, since every possible Q_n is a sum over all particles and can be evaluated while scanning through the events for in principle any number of different harmonics n, followed by plugging all Q-vectors into Eqs. (100) – (102).

4.6.5 Flow Fluctuations

To derive Eqs. (87) – (94) it was assumed that event-by-event fluctuations are negligible and e.g. relations like $\langle v_n^2 \rangle^2 = \langle v_n^4 \rangle$ hold. It is now known that this assumption does not hold and in general $\left\langle v_n^k \right\rangle \neq \langle v_n \rangle^k$ because the flow fluctuations vary the underlying p.d.f. in the average.

To estimate the effect of statistical flow fluctuations to the correlators $\langle\langle m \rangle\rangle$ one can treat $\langle m \rangle$ as a function of a random variable and expand it in a Taylor series around the mean, which gives to leading (second) order in the variance σ_{v_n} respectively [60]

$$\left\langle v_n^2 \right\rangle = \langle v_n \rangle^2 + \sigma_{v_n}^2 \,, \tag{103}$$

$$\left\langle v_n^4 \right\rangle = \langle v_n \rangle^4 + 6\sigma_{v_n}^2 \langle v_n \rangle^2 \,, \tag{104}$$

$$\left\langle v_n^6 \right\rangle = \langle v_n \rangle^6 + 15\sigma_{v_n}^2 \langle v_n \rangle^4 \,, \tag{105}$$

$$\left\langle v_n^8 \right\rangle = \langle v_n \rangle^8 + 28\sigma_{v_n}^2 \langle v_n \rangle^6 \,. \tag{106}$$

Plugging Eqs. (103) – (106) into Eqs. (87) – (94) and assuming a strong flow signal in comparison to the fluctuations $\sigma_{v_n} \ll \langle v_n \rangle$ the to leading order in σ_{v_n} corrected flow coefficients are [60]

$$v_n\{2\} \simeq \langle v_n \rangle + \frac{1}{2}\frac{\sigma_{v_n}^2}{\langle v_n \rangle}\,, \tag{107}$$

$$v_n\{4\} \simeq \langle v_n \rangle - \frac{1}{2}\frac{\sigma_{v_n}^2}{\langle v_n \rangle}\,, \tag{108}$$

$$v_n\{6\} \simeq \langle v_n \rangle - \frac{1}{2}\frac{\sigma_{v_n}^2}{\langle v_n \rangle}\,, \tag{109}$$

$$v_n\{8\} \simeq \langle v_n \rangle - \frac{1}{2}\frac{\sigma_{v_n}^2}{\langle v_n \rangle}\,. \tag{110}$$

It should be noted that in the derivation of these equations no assumptions about the underlying model (i.e. the p.d.f.) of the flow fluctuations were made. A further peculiarity is the fact, that only the 2-particle cumulant is enhanced by flow fluctuations, all other multiparticle cumulants are suppressed. In combination with e.g. Eqs. (84) and (78) this demonstrates that the difference between $v_n\{2\}$ and $v_n\{4\}$ is sensitive to both effects, nonflow and flow fluctuations.

4.6.6 Cumulants vs Nonflow

In section 4.4 the concept of nonflow was introduced, in this section it will be discussed how cumulants behave when nonflow is present.

For “pure” flow it was argued (see section 4.4), that each particle is correlated to a symmetry plane. In combination with cumulants this means that out of M particles in an event one could pick any $c_n\{m\}$ for an arbitrary amount of particles m and since *all* particles of the event (in particular also the m particles picked in the cumulant) are correlated to the symmetry plane, the cumulant will give a non-zero value and hence can measure the collective part (i.e. collective flow). On the other hand an m-particle cumulant will only measure genuine m-particle (and higher) nonflow, since e.g. 2-particle nonflow would not be a genuine m-particle correlation and therefore by definition cannot contribute to all cumulants with $m > 2$. This could be seen e.g. in Eq. (81) where all lower order nonflow contributions canceled.

Considering a simple example of genuine 2-particle nonflow $\delta_{2,n}$, in particular the resonance decay of *one* resonance into two secondary particles, the scaling of its magnitude for an event with multiplicity M can be roughly estimated by combinatorics. Out of the M detected particles the first one is picked and has a chance of $1/M$ of being one of the two correlated by the decay. The second particle is picked out of the remaining $M-1$ particles and has a chance of $1/(M-1)$ of being the second particle of the decay. Thus the total scaling would be

$$\delta_{2,n} \sim \frac{1}{M}\frac{1}{M-1} \sim \frac{1}{M^2} \qquad \text{(one 2-particle resonance decays)}\,. \tag{111}$$

If *every* particle would split into 2 tracks the chance of picking as the first particle a correlated particle is $M/M = 1$ because all particles now come from splitting. The chance for the second particle to be correlated to the first is $1/(M-1)$ giving in total:

$$\delta_{2,n} \sim \frac{1}{M-1} \sim \frac{1}{M} \qquad \text{(M/2 2-particle resonance decays)}\,. \tag{112}$$

For collective flow every particle can be picked as the first one ($M/M = 1$), but since it is correlated to any other due to all being correlated to the symmetry plane ($(M-1)/(M-1) =$

1) the total scaling is unit as it should for collective flow. Similar argumentation [61] gives a scaling of

$$\delta_{4,n} \sim \frac{1}{M}\frac{1}{M-1}\frac{1}{M-2}\frac{1}{M-3} \qquad \text{(one 2-particle resonance decays)}\,, \tag{113}$$

$$\delta_{4,n} \sim \frac{1}{M-1}\frac{1}{M-2}\frac{1}{M-3} \qquad (M/2 \text{ 2-particle resonance decays})\,, \tag{114}$$

for the 4-particle cumulant.

An example for the latter scaling in experiments could be the process $\rho \to \pi\pi$, from which a significant fraction of the produced pions originates. The scaling Eq. (112) together with Eq. (30) gives also a hint on when nonflow can be neglected in 2-particle correlations, namely when $v_n \gg M^{-1/2}$.

The nonflow scaling with multiplicity is important to estimate for up to which M $v_n\{m\}$ is still reliable. The condition is that the flow signal has to be (much) bigger than the nonflow contribution:

$$\left\langle v_n^2 \right\rangle \overset{!}{\gg} \frac{1}{M} \quad \Rightarrow \quad v_n \gg \frac{1}{M^{1/2}}\,, \tag{115}$$

$$\left\langle v_n^4 \right\rangle \overset{!}{\gg} \frac{1}{M^3} \quad \Rightarrow \quad v_n \gg \frac{1}{M^{3/4}}\,. \tag{116}$$

It is easily visible that the 4-particle flow estimator scales much milder and is sooner a reliable estimate for the true flow coefficient (for typical M in Pb-Pb collisions see Fig. 12 or 15).

In principle all sorts of possible nonflow sources could be derived in an analytic way (e.g. k-times track splitting by weighting the Q-vector k times), for some examples see [60, 61]. Furthermore a way to quickly estimate many sorts of nonflow contributions is by using Monte Carlo simulations, but in general there is currently no systematic way to eliminate them all exactly.

5 Results / Data Analysis

5.1 Used Data and Quality Assurance

The data used in this thesis stem from the ALICE experiment at the LHC at CERN. It consists of two datasets of Pb-Pb collisions recorded for different beam energies. The first set, hereinafter referred to as Run 1, was recorded in November 2010 and was taken at a center of mass energy of $\sqrt{s_{NN}} = 2.76\,\mathrm{TeV}$ per nucleon pair. The second dataset, hereinafter referred to as Run 2, is from the end of 2015 and was taken at a center of mass energy of $\sqrt{s_{NN}} = 5.02\,\mathrm{TeV}$. In total the Run 1 dataset has about 100 000 events and the Run 2 set about 70 000 events, which is only a small percentage of the total data taken by the ALICE Collaboration and thus some analyses are lacking statistics. This is also why only the statistical errors, which are considerably larger than the systematic ones [117, 118], are shown in the following results. Both datasets are structured in the same way: For each event a list of non-identified particles with corresponding kinematic variables azimuthal angle φ, transverse momentum p_{T} and pseudorapidity η is given. The events came pre-binned in centrality classes, which was done using AliRoot's [119] standard centrality determination framework[27] (for detailed description see [56, 120]).

For the reconstruction the TPC as well as the ITS were used as the main tracking devices, reconstructing so called *global tracks*. Because in flow analyses any inefficiencies in the detector's azimuthal acceptance will introduce a non-negligible bias, one either has to have a uniform distribution or use acceptance corrected formulas (see for example [60, 102]). Azimuthal distributions of all reconstructed particles are shown in Fig. 11, indicating close to uniform distributions and thus making it unnecessary to correct for non-uniform acceptance.

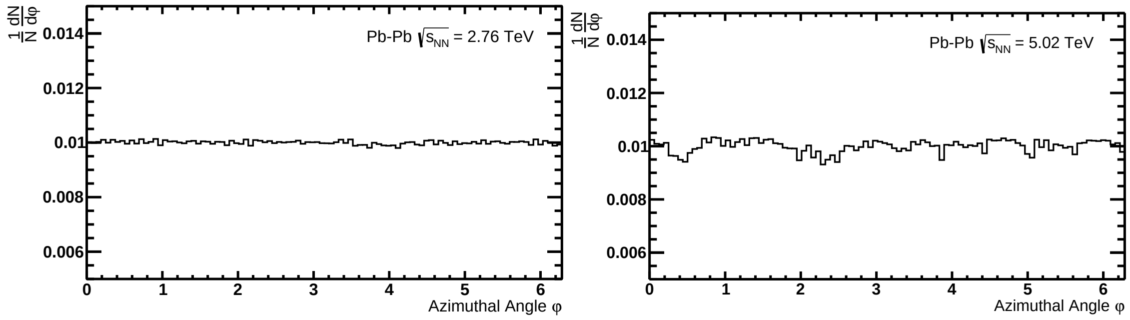

(a) (b)

Figure 11: Azimuthal distribution of all reconstructed particles for **a)** Run 1 and **b)** Run 2 data, for $0.2 < p_{\mathrm{T}} < 5.0\,\mathrm{GeV}/c$ and $|\eta| < 0.8$.

The kinematic region was cut to $0.2 < p_{\mathrm{T}} < 5.0\,\mathrm{GeV}/c$ for the transverse momentum and to $|\eta| < 0.8$ for the pseudorapidity. As mentioned in section 2 the tracking capability below $0.2\,\mathrm{GeV}/c$ decreases significantly, since a large number of particles in this momentum region cannot even fully reach and traverse the TPC. The upper p_{T} boundary is due to the increasing probability of jets[28] being produced, which highly affect nonflow. Physical

---

[27] Which is basically fitting a Glauber model to the multiplicity measured with VZERO.

[28] Jets are narrow cones of high p_{T} particles, which are created when a very high p_{T} parton (carrying color charge) is produced in a collision and then hadronizes. Because of QCD confinement (see section 1) the parton creates other colored objects around itself which are boosted in the parton's direction. The collective cone of produced particles is called jet and induces strong correlations. These correlations heavily

acceptance of the TPC, which per design is limited to $|\eta| < 0.9$ and with the requirement of uniform acceptance to $|\eta| < 0.8$, explain the pseudorapidity range. The requirement of uniform acceptance limits the $|\eta|$ range to 0.8 instead of 0.9, because after primary vertex determination with the help of the SPD, which has a resolution of $10\,\mu$m [63], events are allowed in the range of $|z| < 10\,$cm.

The multiplicity distributions for this kinematic region are shown in Fig. 12. They show higher probability for low multiplicity events, exhibiting a plateau like trend before quickly dropping at a maximum multiplicity. The graph can easily be understood in terms of the collision geometry: Highest multiplicity events stem from the most central collisions which are much more unlikely to happen than peripheral. For Run 1 with $\sqrt{s_{NN}} = 2.76\,$TeV a maximum of about 2600 particles per event can be produced and tracked. This maximum increases to about 2900 particles per event at Run 2 energies of $\sqrt{s_{NN}} = 5.02\,$TeV.

The transverse momentum distributions, respectively for Run 1 and 2 shown in Fig. 13 a) and b), show a maximum number of detected charged particles for the lowest measured p_{T}. With increasing p_{T} the probability (i.e. the number of detected particles) decreases nearly exponentially until reaching the kinematic cutoff at $p_{\mathrm{T}} = 5.0\,$GeV. In comparison with Run 1 at $\sqrt{s_{NN}} = 2.76\,$TeV the transverse momentum distribution at $\sqrt{s_{NN}} = 5.02\,$TeV has the same course but with slightly increased mean p_{T}.

The pseudorapidity distribution, which is shown in Fig. 14 a) for Run 1 and in Fig. 14 b) for Run 2, has a close to uniform distribution with an exception at mid-rapidity where it shows a slight valley. This might be due to a reconstruction efficiency of the TPC close to $\eta = 0$, but should not influence flow measurements.

The per centrality multiplicity distributions, shown in Fig. 15, reveal that for more central collisions not only more particles are produced per event, but also in a wider multiplicity range around a mean. This mean shifts to higher multiplicities for more central events, while at the same time broadening but shrinking. Special attention has to be payed to events which considerably deviate in multiplicity from the otherwise concentrated peak-like distribution. In a flow analysis these outlier events, often referred to as “grass”, might impact the analysis depending on whether their multiplicity is higher or lower than the typical multiplicity for a given centrality. The reasoning lies in the weighting factor of the all event averages of multiparticle correlators one has to perform in flow analysis. As argued before the weight has to be the number of distinct k-particle combinations one can form for an event with multiplicity M, thus events with higher M are weighted much stronger ($\sim M^k$). On the other hand low multiplicity events contribute very little to the average and do not distort the results. The data shown in Fig. 15 shows only low M grass and is thus suitable for further analyses.

5.2 Elliptic Flow v_2

In the following the elliptic flow v_2 will be analyzed in more detail, by looking at the v_2 dependence on centrality and different kinematic variables like pseudorapidity η and transverse momentum p_{T}.

5.2.1 Centrality Dependence

Figure 16 shows the centrality dependence of elliptic flow v_2 estimated with 2- and multi-particle cumulants for Run 1 energies $\sqrt{s_{NN}} = 2.76\,$TeV shown in Fig. 16 a) and Run 2 energies $\sqrt{s_{NN}} = 5.02\,$TeV shown in 16 b). The centrality is binned into 9 different centrality classes, as described in section 1.3.1, ranging from 0% (central) to 80% (peripheral) with

---

contribute to nonflow and are treated as systematic bias in flow analyses.

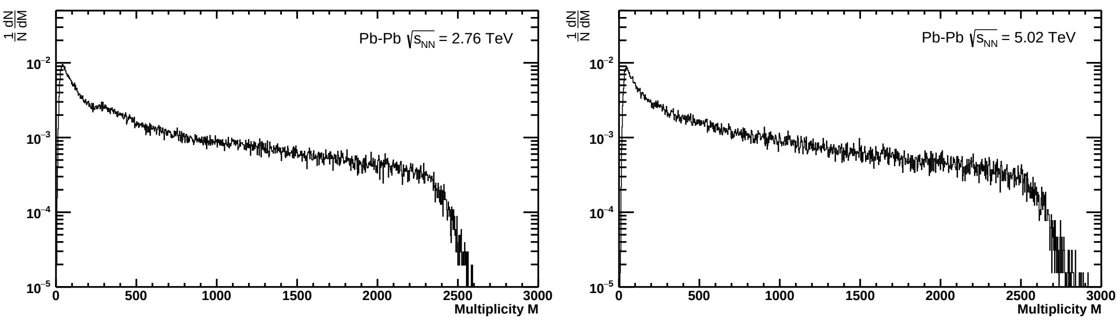

(a) (b)

Figure 12: The multiplicity distribution of all reconstructed particles for **a)** Run 1 and **b)** Run 2 data, for $0.2 < p_{\mathrm{T}} < 5.0\,\mathrm{GeV}/c$ and $|\eta| < 0.8$.

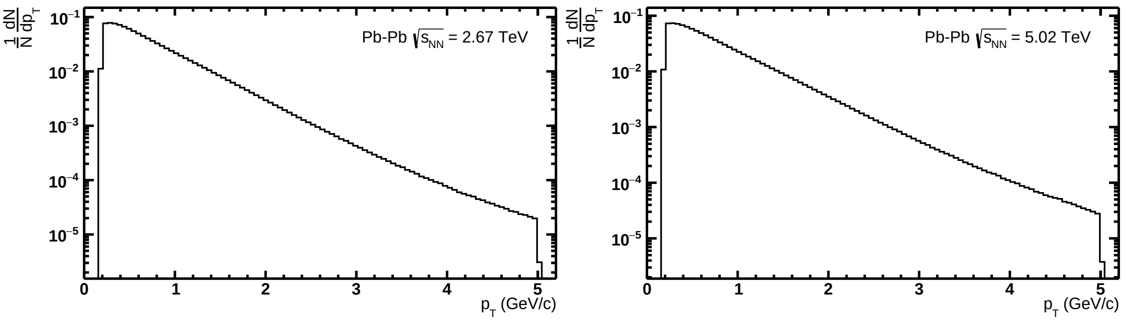

(a) (b)

Figure 13: The transverse momentum distribution of all reconstructed particles for **a)** Run 1 and **b)** Run 2 data, for $|\eta| < 0.8$.

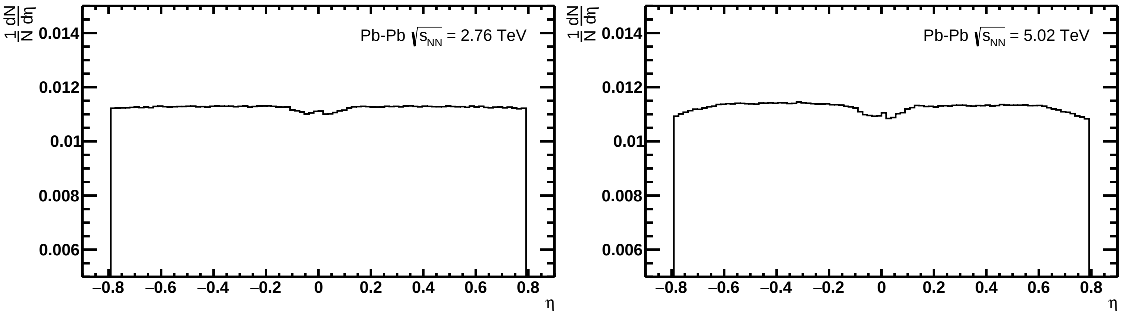

(a) (b)

Figure 14: The pseudorapidity distribution of all reconstructed particles for **a)** Run 1 and **b)** Run 2 data, for $0.2 < p_{\mathrm{T}} < 5.0\,\mathrm{GeV}/c$.

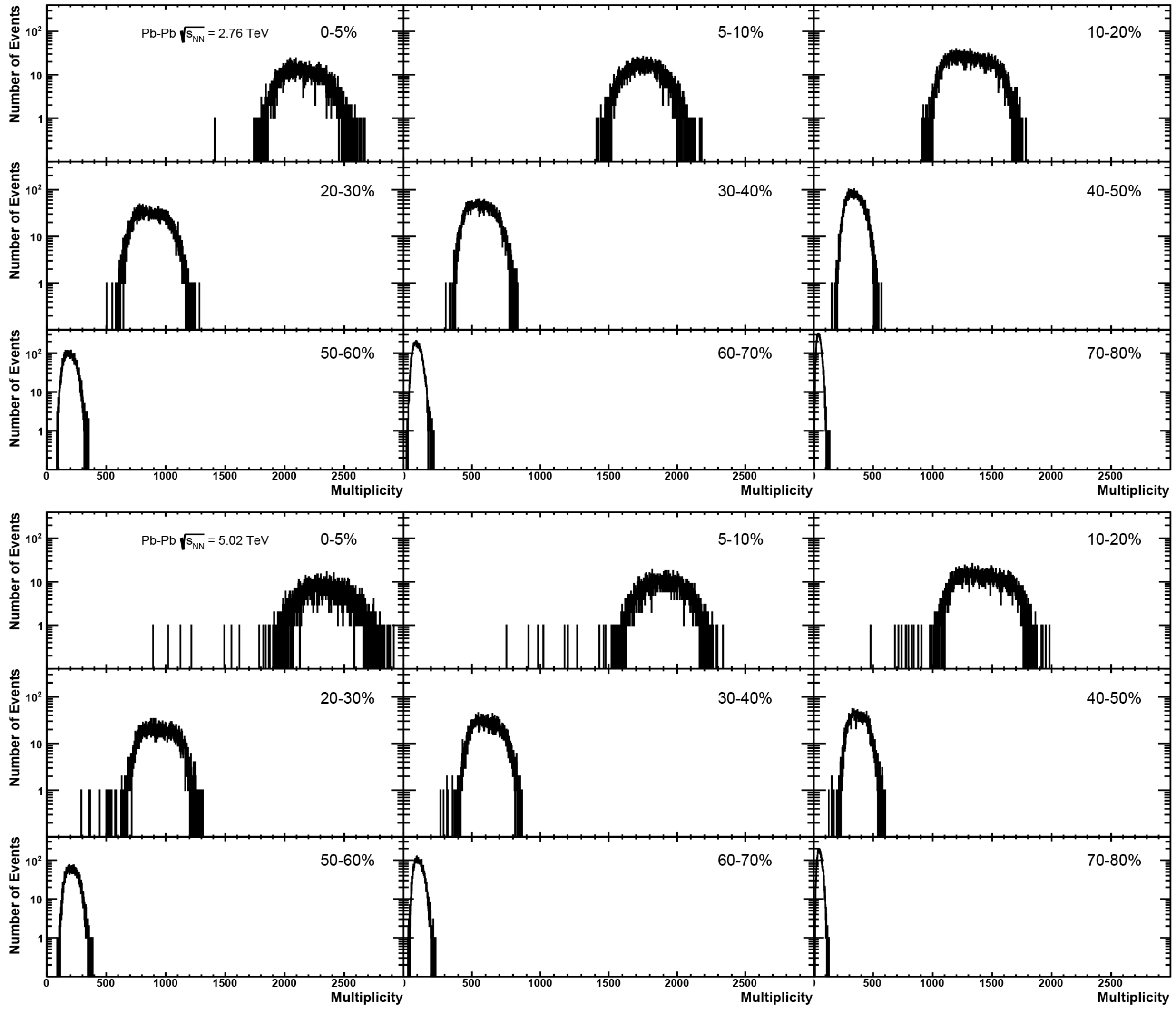

Figure 15: The multiplicity distribution of all reconstructed particles per centrality class for **top:** Run 1 and **bottom:** Run 2 data, for $0.2 < p_{\mathrm{T}} < 5.0\,\mathrm{GeV}/c$ and $|\eta| < 0.8$.

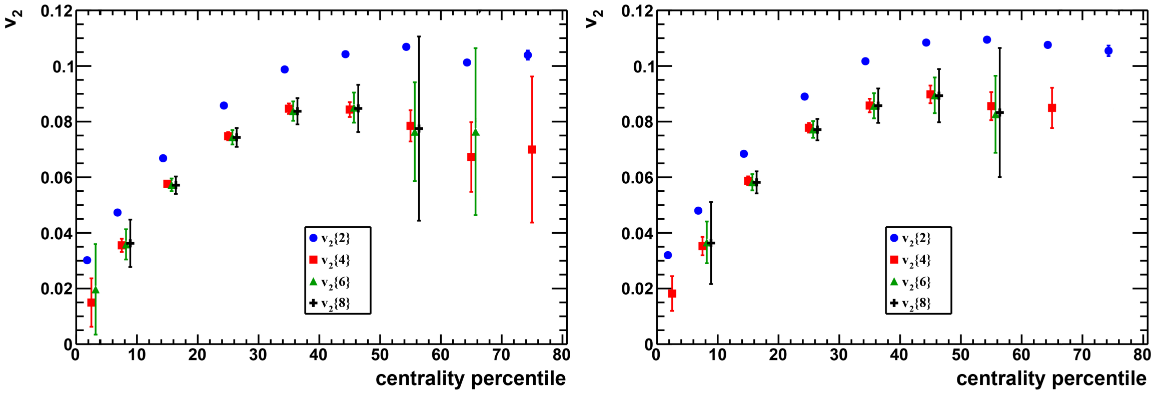

(a) (b)

Figure 16: Centrality dependence of elliptic flow, integrated in the p_T range of $0.2 < p_\mathrm{T} < 5.0\,\mathrm{GeV}/c$ and estimated with two- and multiparticle correlation techniques for **a)** Run 1 and **b)** Run 2. (Data points are shifted horizontally for visibility.)

a bin width of 10% (except for the 0-10% bin which is subdivided at 5%). The different marker colors indicate the number of particles used to estimate the elliptic flow, starting at 2-particle correlations and going up to eight particles. Since systematic errors are not dominant [121] (especially with the limited statistics), the shown errors are purely statistical and also do not include covariance terms, which would contribute with a minus sign, thus lowering the errors. In general a strong centrality dependence of elliptic flow can be seen, starting with v_2 values smaller than 0.02 for most central collisions, quickly increasing with growing centrality up to a maximum of about 0.1 around 50% and then starting to slowly decrease again for the peripheral collisions. The low initial values and subsequent rise in elliptic flow can be understood in terms of initial geometrical overlap. For central collisions the, to leading order, ellipsoidal overlap region is not appropriately anisotropic but is almost circular. The decreasing elliptic flow for peripheral collisions is due to the limited area of overlap. Only a small number of partons interact, leading to a system which is to small to properly thermalize. A significant splitting between flow estimated from two- and multiparticle correlations is visible. This splitting arises from event-by-event fluctuating flow values as well as nonflow contributions. Statistical flow fluctuations contribute, to leading order, with a plus sign for the 2-particle cumulant flow estimator and with a minus sign to all higher order cumulants (see section 4.6.5). As discussed in section 4.6.6, 2-particle correlations are plagued by nonflow, whereas multiparticle correlations systematically suppress nonflow. This argumentation is consistent with the results in a sense, that all multiparticle flow estimates agree within errors. In particular 6- and 8- particle estimates are in excellent agreement with the 4-particle estimate, indicating that already 4-particle cumulants suppress nonflow significantly. Furthermore this implies, that the “true” flow value has to lie between the 2-particle estimate and the multiparticle estimate, but more towards the multiparticle result, since this is less influenced by nonflow.

To compare the results at $\sqrt{s_{NN}} = 2.76\,\mathrm{TeV}$ and $\sqrt{s_{NN}} = 5.02\,\mathrm{TeV}$, differences get more clear by taking the ratios as shown in Fig. 17. The left plot shows v_2 estimated via 2-particle correlations as a function of centrality, as well as the ratio between v_2 in Run 1 and Run 2, fitted with a constant. The right plot shows the same information but for elliptic flow estimated via 4-particle correlations. Both flow estimates show an increase in elliptic flow going from Run 1 to Run 2 energies, which is, independently of the centrality, flat within

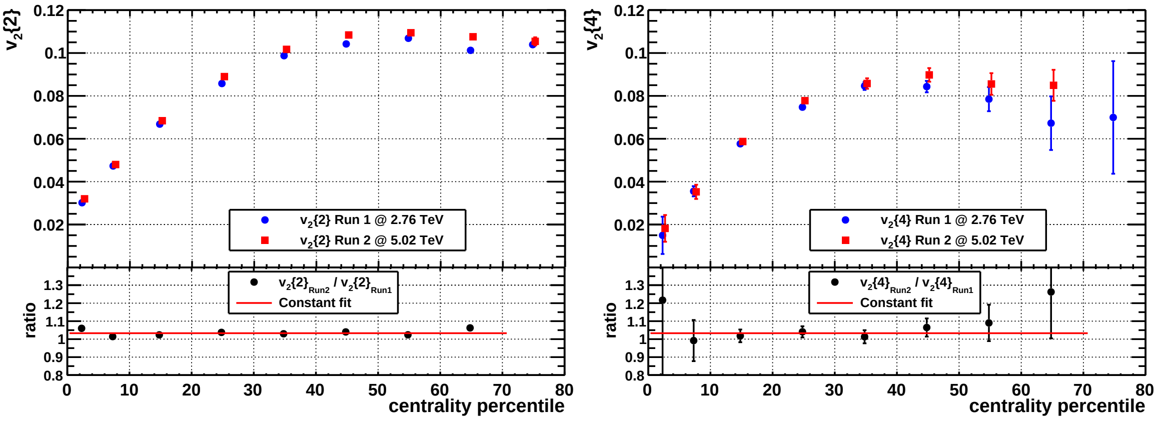

(a) (b)

Figure 17: Ratios of elliptic flow v_2 measured in Run 1 and Run 2, estimated with **a)** 2-particle correlations and **b)** 4-particle correlations. (For the fit values see text.)

the errors. Quantitatively, $v_2\{2\}$ increased by $3.30 \pm 0.31\,\%$ and $v_2\{4\}$ by $3.29 \pm 1.77\,\%$.

5.2.2 Transverse Momentum Dependence

Instead of integrating over a transverse momentum range, it is also interesting to do a p_{T} differential flow analysis. Elliptic flow as a function of p_{T}, estimated from 2- up to 8-particle correlations (where numerically feasible) in various centrality classes for Run 1 as well as Run 2 is shown in Fig. 18. The binning, indicated by horizontal error bars, was chosen in such a way, that each bin has approximately the same amount of particles and hence statistics. It can be seen that for most centrality classes there is not enough statistics needed for the higher order cumulants, therefore the same analysis is done in Fig. 19, but only for the 2-particle flow estimator, however with finer binning. Throughout all centralities the elliptic flow starts to increase linearly for low p_{T}, but saturates starting around $p_{\mathrm{T}} \approx 2.0\,\mathrm{GeV}/c$. Over the measured p_{T} range the differential flow magnitude for a given centrality class is proportional to the centrality dependence shown in Fig. 16, however if one would measure the flow for even higher p_{T} than $5.0\,\mathrm{GeV}/c$ the possibility of jets increases, which would pollute the pure flow signal[29].

The transverse momentum dependence of flow is also interesting, because it probes the hydrodynamic picture. Hydrodynamics as an effective theory successfully describing collective properties of the produced system cannot model high p_{T} particles, which are fast enough to escape the created medium before reaching equilibrium. This can be used as an estimate up to which p_{T} hydrodynamics is applicable and also explains the flow saturation.

Although the center of mass energy nearly doubled between Run 1 and 2 and integrated flow as a function of centrality increased in all centrality classes by about 3%, an increase in p_{T} differential flow cannot be seen. Therefore the increase in integrated flow should be

---

[29] In fact, after the saturation region the p_{T} differential flow eventually starts to decrease again, but will keep a decently large magnitude (≈ 0.1) even up to $p_{\mathrm{T}} \approx 20.0\,\mathrm{GeV}/c$ [122], which is not due to the expansion of a thermalized system, but due to the dominance of high energy parton fragmentation. Produced in hard initial scatterings, these partons traverse the nuclear matter, loosing energy depending on the path length (and color charge density of the medium), which again is dependent on azimuthal emission angle [53]. This phenomenon of jet quenching introduces an azimuthal momentum space anisotropy for high p_{T} and thus nonzero contribution to 2- and multiparticle azimuthal correlations.

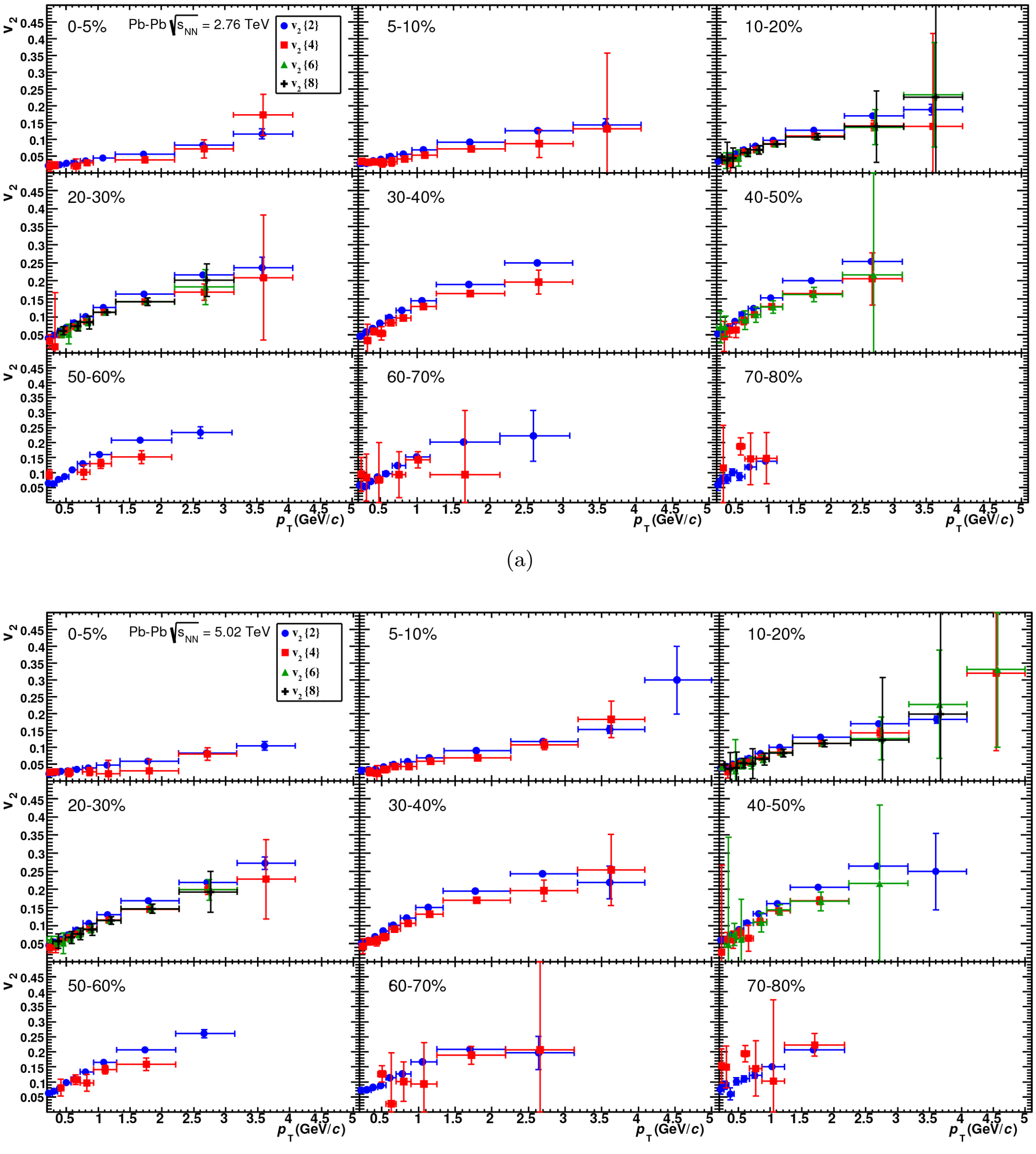

(a)

(b)

Figure 18: Transverse momentum dependence of elliptic flow v_2 estimated with two- and multiparticle correlation techniques, presented for different centrality classes for **a)** Run 1 and **b)** Run 2. (Data points are shifted horizontally for visibility.)

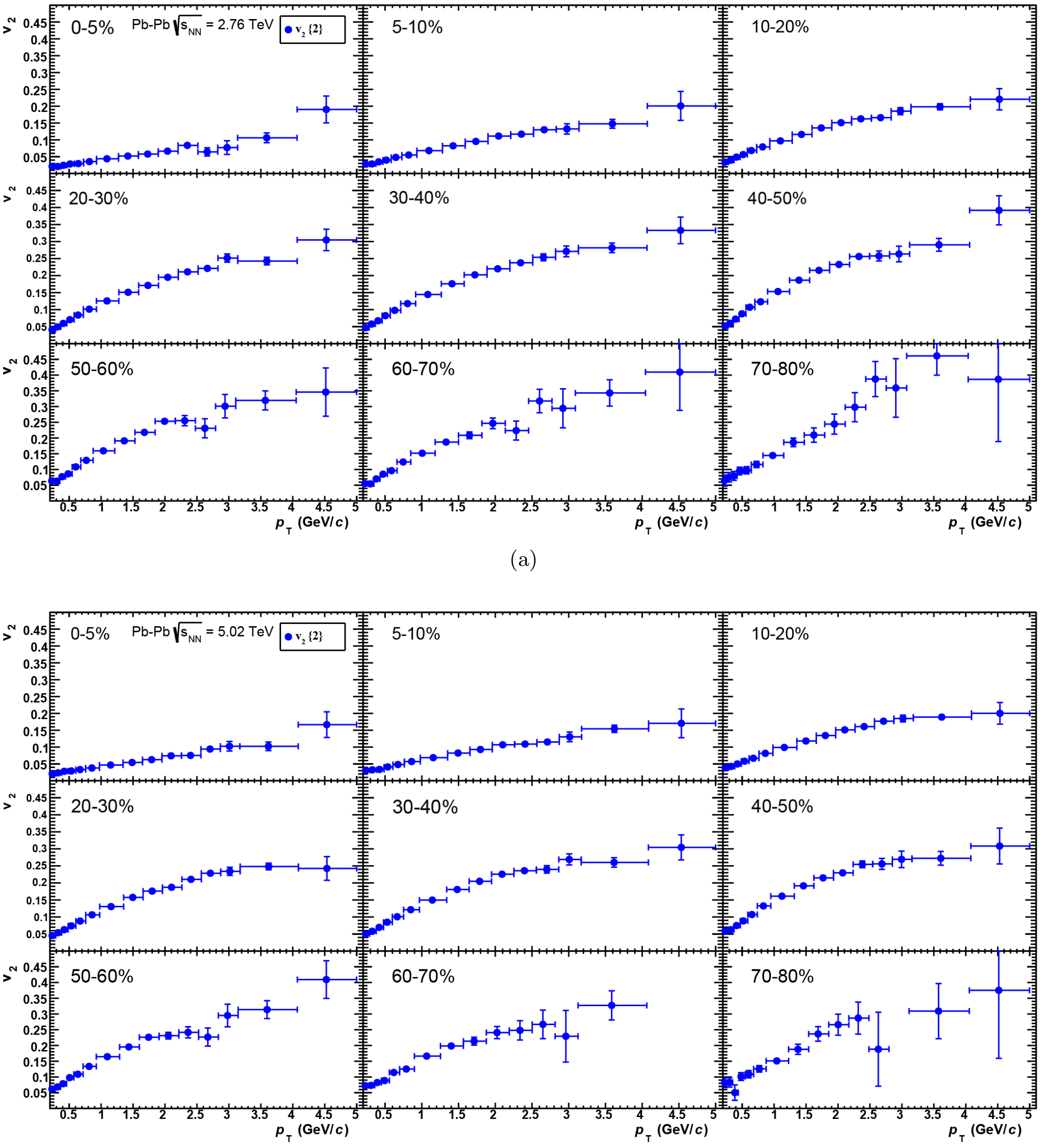

(a)

(b)

Figure 19: Transverse momentum dependence of elliptic flow v_2 estimated with two-particle correlation techniques, presented for different centrality classes for **a)** Run 1 and **b)** Run 2.

due to an increase in mean transverse momentum $\langle p_\mathrm{T} \rangle$ [123], which implies an increase in radial flow [118].

5.2.3 Pseudorapidity Dependence

In Fig. 20 differential elliptic flow as a function of pseudorapidity η, estimated with up to 8-particle correlations (where numerically feasible) is shown for different centrality classes for Run 1 and Run 2 data. It is observed that in the measured pseudorapidity range of $|\eta| < 0.8$ elliptic flow exhibits very little pseudorapidity dependence and stays constant within the statistical errors. Just as for the p_T dependence, the per centrality mean flow develops as expected from Fig. 16 and a splitting between 2- and multiparticle correlations due to flow fluctuations is visible.

An η differential analysis can help to understand flow contributions from different stages of the collision evolution. This is because at larger $|\eta|$ the multiplicity density becomes smaller, which corresponds to a smaller initial entropy density, which in turn means sooner hadronization of the strongly interacting medium [61].

Since in Fig. 20 it was observed that v_2 stays constant as a function of pseudorapidity (in the measured range), this result can be used to estimate nonflow. As already indicated in section 4.6.6 nonflow of a 2-particle correlation scales roughly like $1/M$. Figure 21 shows the elliptic flow pseudorapidity dependence estimated with 2-particle correlations, but binned in two different ways. In the left plot the binning was done equally in 0.2 width bins. The right plot however has increasing bin sizes or in other words η integrated flow. Here all bins start at -0.8 but increase by 0.2 per bin, i.e. the third marker has a bin width of -0.8 to -0.2 . As a consequence the multiplicity increases leading to a decrease of $v_2\{2\}$ with roughly $1/M$. Since $v_2\{2\}$ vs η is flat, any change in flow is now due to nonflow, which is visible as a slope in Fig. 21 b).

5.3 Higher Harmonics

In addition to the detailed elliptic flow studies presented in this thesis also higher harmonics were measured. In particular triangular flow v_3, quadrangular flow v_4, pentagonal flow v_5 and hexagonal flow v_6, which progressively decrease in the magnitude of the flow signal. Fig. 22 shows these higher flow harmonics as a function of centrality. All four coefficients show an increase with centrality, however not as steep as v_2. If v_2, which is assumed to mainly arise from the anisotropic overlap shape, is compared with e.g. v_3, which on the other hand is assumed to arise solely from fluctuations, it can be seen that for ultra-central collisions where the overlap is close to isotropic both have about equal magnitude. Compared between Run 1 and Run 2 v_3 and v_4 show an increase in all centralities, although for v_4 it increased especially in central collisions. The next two flow coefficients v_5 and v_6 seem to also increase, but for in higher centrality percentiles errors become too big to give a clear interpretation. Respectively the over the centrality range 0-70% fitted values show an flow increase of $(7.70 \pm 0.71)\%$ for v_3, $(19.76 \pm 1.62)\%$ for v_4, $(7.88 \pm 3.94)\%$ for v_5 and $(24.22 \pm 6.48)\%$ for v_6. Since all flow coefficients were estimated with 2-particle cumulants, due to insufficient statistics for multiparticle correlators, the value is nonflow and fluctuation biased (see discussion in section 4.6.5 and 4.6.6) leading in general for the 2-particle estimate to higher values than the true one.

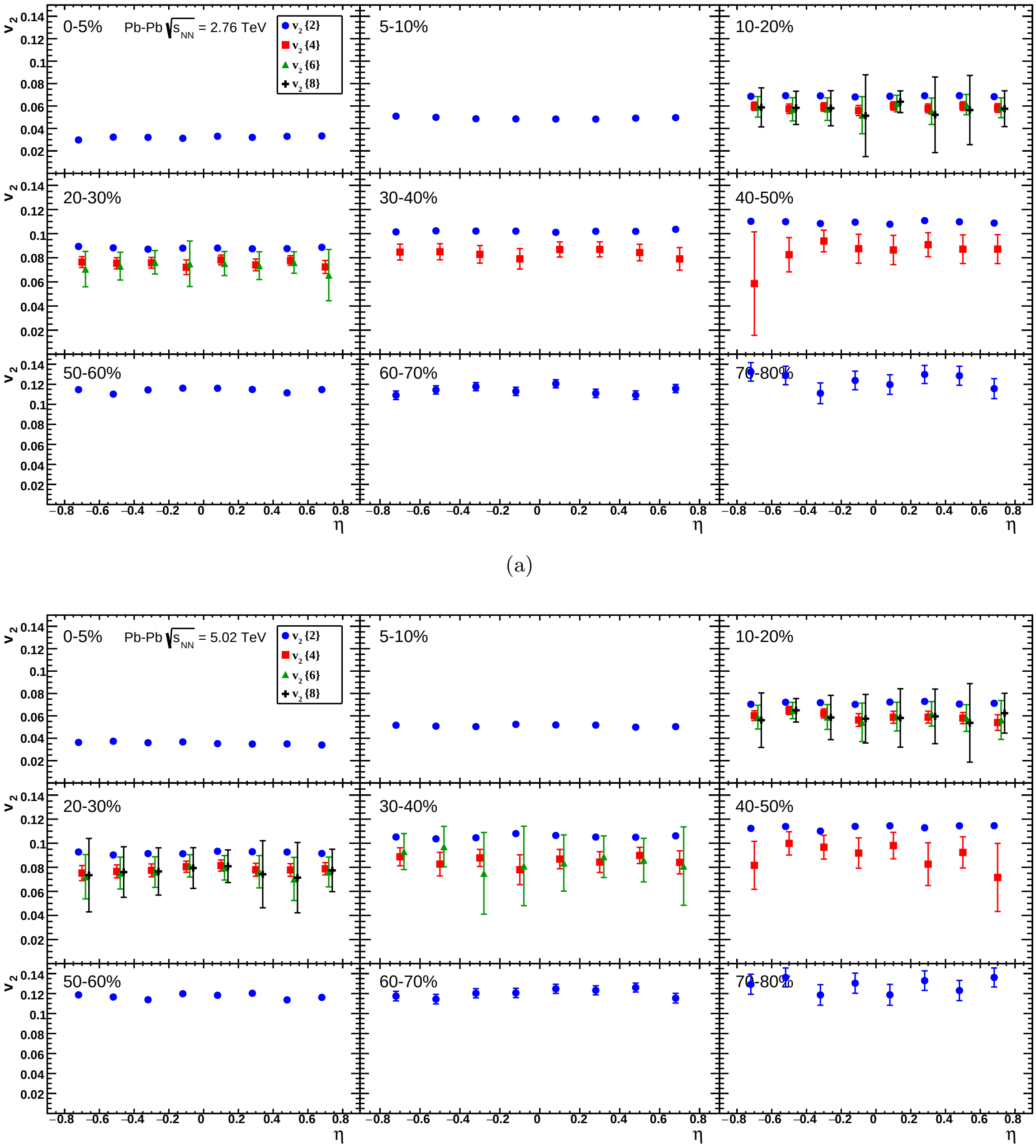

(a)

(b)

Figure 20: Pseudorapidity dependence of elliptic flow v_2 estimated with two- and multiparticle correlation techniques, presented for different centrality classes for **a)** Run 1 and **b)** Run 2.

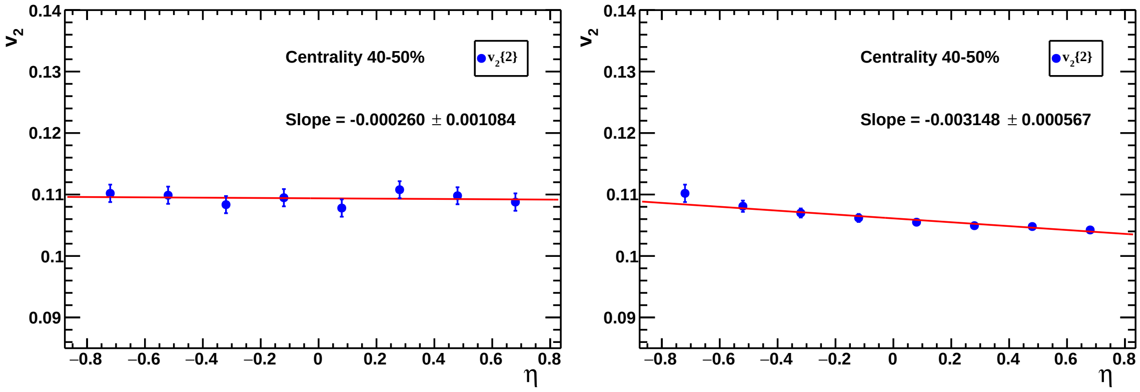

(a)

(b)

Figure 21: Pseudorapidity dependence of elliptic flow v_2 estimated with two-particle correlation techniques, at $\sqrt{s_{NN}} = 2.76\,\text{TeV}$ and 40-50% centrality. Figure **a)** has constant bin widths of 0.2, figure **b)** has bin widths which all start at -0.8 and increase by 0.2 per bin.

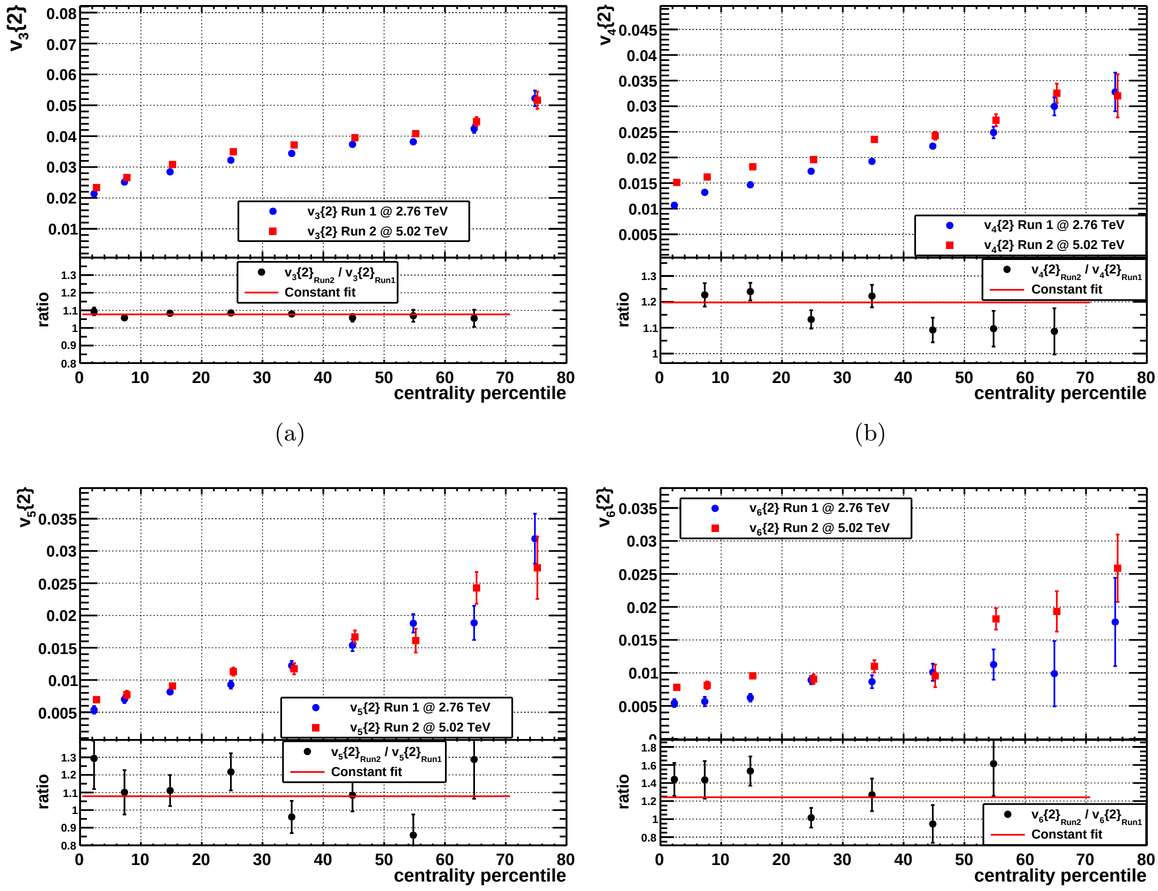

(a)

(b)

(c)

(d)

Figure 22: **a)** Triangular flow v_3, **b)** quadrangular flow v_4, **c)** pentagonal flow v_5 and **d)** hexagonal flow v_6 as a function of centrality and their corresponding ratios between Run 1 and Run 2, estimated with 2-particle correlations. (For the fit values see text.)

6 Symmetry Plane Correlations (SPC)

As indicated in section 3.1.2 and 3.1.3 the flow field is steering into an era of event-by-event fluctuations, which are caused by the fluctuations in the initial nucleon and parton density distributions of the colliding nuclei. Event-by-event measurements lead to many new observables, because they not only give information about all event averaged quantities like $\langle v_n \rangle$, but measure the underlying p.d.f., examples which are under investigation are flow distributions $\mathrm{p}(v_n)$ [124], flow amplitude correlations $\mathrm{p}(v_n, v_m)$, symmetry plane correlations $\mathrm{p}(\Psi_n, \Psi_m, \dots)$ [125], mixed correlations $\mathrm{p}(v_l, \Psi_n, \Psi_m, \dots)$ [126]. This section will focus on symmetry plane correlations, which open new degrees of freedom apart from the flow coefficients in the Fourier series. A general overview of existing methods is not given (for this see e.g. [126],[127]), but instead novel observables will be presented. The prevailing question in this section is therefore how to measure pure symmetry plane correlations without mixed effects of flow harmonics and how to achieve this goal using multiparticle correlation techniques.

6.1 Constructing the Observables

Starting with an mixed harmonic m-particle correlator, it can be rewritten [85] as

$$\begin{aligned}\left\langle\left\langle e^{i(n_1\varphi_1+n_2\varphi_2+\dots+n_m\varphi_m)}\right\rangle\right\rangle &= \left\langle\left\langle e^{in_1\varphi_1}\right\rangle\left\langle e^{in_2\varphi_2}\right\rangle\dots\left\langle e^{in_m\varphi_m}\right\rangle\right\rangle + \text{nonflow} && (117)\\ &= \left\langle v_{n_1}e^{in_1\Psi_{n_1}}v_{n_2}e^{in_2\Psi_{n_2}}\dots v_{n_m}e^{in_m\Psi_{n_m}}\right\rangle + \text{nonflow} && (118)\\ &= \left\langle v_{n_1}v_{n_2}\dots v_{n_m}e^{i\left(n_1\Psi_{n_1}+n_2\Psi_{n_2}+\dots+n_m\Psi_{n_m}\right)}\right\rangle + \text{nonflow} && (119)\end{aligned}$$

where the inner brackets indicate an average over all m particles in an event and the outer brackets an average over all events, thus the harmonics have to be isotropic $\sum_i n_i = 0$ to not trivially average to 0 in the all event average, i.e. invariance under global phase shift holds $\Psi_i \to \Psi_i + \alpha\ \forall i \in [1, m]$. Furthermore symmetry plane Ψ_n has an n-fold symmetry and should therefore be invariant under phase shifts $\Psi_n \to \Psi_n + 2\pi/n$. It is reminded that the LHS of Eq. (119) can be calculated using multiparticle cumulants, also in event-by-event analyses (for the generic framework see [102]). For idealized initial geometry all symmetry planes Ψ_n coincide and the imaginary part of Eq. (119) is identically zero for isotropic correlators (see section 3.1.2).

In recent studies [125] an adjusted and resolution corrected version of the event plane method was used, as well as a scalar product method. Following the discussion of section 4.2 these methods (especially the EP method) should be avoided, therefore in the following methods making use of multiparticle cumulants are introduced.

6.2 “Ratio Method”

The idea of this method is to use Eq. (119) and take event-by-event a ratio of multiparticle correlators expressed in mixed harmonics, choose in such a way that the flow harmonics cancel and the symmetry correlation part in the denominator equals 1. To clarify this concept an example using 6-particle correlators is given:

$$\frac{\Big\langle \exp\big[in\left(+2\varphi_1+2\varphi_2-1\varphi_3-1\varphi_4-1\varphi_5-1\varphi_6\right)\big]\Big\rangle}{\Big\langle \exp\big[in\left(+2\varphi_1-2\varphi_2+1\varphi_3-1\varphi_4+1\varphi_5-1\varphi_6\right)\big]\Big\rangle} \tag{120}$$

$$=\frac{v_{2n}^2 v_n^4 \exp\big[in\left(2\Psi_{2n}+2\Psi_{2n}-1\Psi_{1n}-1\Psi_{1n}-1\Psi_{1n}-1\Psi_{1n}\right)\big]}{v_{2n}^2 v_n^4 \exp\big[in\left(2\Psi_{2n}-2\Psi_{2n}+1\Psi_{1n}-1\Psi_{1n}+1\Psi_{1n}-1\Psi_{1n}\right)\big]} \tag{121}$$

$$=\frac{\exp\big[i4n\left(\Psi_{2n}-\Psi_n\right)\big]}{\exp[0]} \tag{122}$$

$$=\exp\big[i4n\left(\Psi_{2n}-\Psi_n\right)\big] \tag{123}$$

This expression has the wanted effect of removing on a per event basis flow magnitude contributions while correlating a symmetry plane in harmonic n with another plane of harmonic $2n$. One notices that for the denominator SPC to vanish each harmonic has to be taken an even amount of times, each half of the particles with opposite sign, while in the numerator every isotropic combination of harmonics is possible. A mathematical expression can be derived for a general (kn, n) SPC

$$\exp\big[i2kn\left(\Psi_{kn}-\Psi_n\right)\big]=\frac{\left\langle \exp\left[n\left(k\varphi_1+k\varphi_2-\sum_{j=3}^{2k+2}\varphi_j\right)\right]\right\rangle}{\left\langle \exp\left[n\left(k\varphi_1-k\varphi_2+\sum_{j=3}^{2k+2}(-1)^j\varphi_j\right)\right]\right\rangle} \tag{124}$$

as well as for a type (kn, mn, n) SPC where it is w.l.o.g. assumed that $k > m$

$$\exp\Big[i2n\left(k\Psi_{kn}-m\Psi_{mn}-(k-m)\Psi_n\right)\Big]=\frac{\left\langle \exp\left[n\left(k\varphi_1+k\varphi_2-m\varphi_3-m\varphi_4-\sum_{j=5}^{2(k-m)+4}\varphi_j\right)\right]\right\rangle}{\left\langle \exp\left[n\left(k\varphi_1-k\varphi_2-m\varphi_3+m\varphi_4+\sum_{j=5}^{2(k-m)+4}(-1)^j\varphi_j\right)\right]\right\rangle}. \tag{125}$$

To find the minimal SPC the number of m-terms N_m has to be maximized and hence has to be the closest even number that fulfill $N_m = 2\frac{k-1}{m}$.

In theory in such a way any amount of particles can be used in the correlator, however in practice experience tells a feasible order up to about 14 particles. Formulas for 2- and 3-SPC were given, but to achieve higher order SPC higher order correlators are needed. In particular to achieve a 4-SPC 8-particle correlators are needed, for 5-SPC 10-particle, etc.

Furthermore other constructions using correlators are possible, for example it in not mandatory to use a correlator of the same order in the denominator as in the numerator. The denominator could consist of more than one correlator, though the same order might be the better choice because in that way both numerator and denominator are influenced in the same way by effects like nonflow.

6.3 "Normalization and Phase Method"

The idea of these two methods lie in the properties of complex numbers. In the first method the SPC is obtained by plain normalization of the correlator, hence canceling the flow magnitudes, again event-by-event:

$$\frac{\left\langle e^{-i(n_1\varphi_1+...+n_k\varphi_k)}\right\rangle}{\left|\left\langle e^{-i(n_1\varphi_1+...+n_k\varphi_k)}\right\rangle\right|} = e^{i\left(n_1\Psi_{n_1}+...+n_k\Psi_{n_k}\right)}\,. \tag{126}$$

A problem with this procedure is that the normalization prevents the real part from fluctuating past ±1 and therefore systematically biases the estimate.

The second method also takes advantage of fundamental properties of complex numbers, namely the argument, which is used to extract the phase:

$$n_1\Psi_{n_1} + ... + n_k\Psi_{n_k} \tag{127}$$

$$= \arg\left[\left\langle e^{-i(n_1\varphi_1+...+n_k\varphi_k)}\right\rangle\right] \tag{128}$$

$$= \operatorname{atan2}\Big(\mathfrak{Im}\big\langle\exp(-i\,[n_1\varphi_1 + ... + n_k\varphi_k])\big\rangle, \mathfrak{Re}\,\big\langle\exp(-i\,[n_1\varphi_1 + ... + n_k\varphi_k])\big\rangle\Big) \tag{129}$$

The problem here is similar, the phase is limited to the interval $[0, 2\pi)$ and unfolding problems arise.

6.4 Flow Scaling and Optimizer

The error σ_{v_n} of a per-event flow estimate using an m-particle correlator scales roughly like

$$\sigma_{v_n} \sim \frac{1}{M^{m/2}}\frac{1}{v_n^{m-1}} \tag{130}$$

where M is the multiplicity, n the harmonic and m the number of particles used to construct the correlator. Since the SPC methods presented in this thesis are based on multiparticle correlators this scaling can be used to investigate how to modify them in order to reduce the error. This leads to the concept of *optimizer*. Analytically there infinitely many correlator ratios yielding the same observable, e.g. coming back to the example Eq. (120) a second ratio can be constructed

$$\frac{\Big\langle\exp\big[in\,(+2\varphi_1 + 2\varphi_2 - 1\varphi_3 - 1\varphi_4 - 1\varphi_5 - 1\varphi_6 + 2\varphi_7 - 2\varphi_8)\big]\Big\rangle}{\Big\langle\exp\big[in\,(+2\varphi_1 - 2\varphi_2 + 1\varphi_3 - 1\varphi_4 + 1\varphi_5 - 1\varphi_6 + 2\varphi_7 - 2\varphi_8)\big]\Big\rangle} \tag{131}$$

$$= \underbrace{\frac{v_{2n}^2}{v_{2n}^2}}_{\text{new}}\,\frac{v_{2n}^2 v_{4n}^4}{v_{2n}^2 v_{4n}^4}\,\frac{\cos(4n[\Psi_{2n} - \Psi_n])}{\cos(0)} \tag{132}$$

$$= \exp\big[i4n\,(\Psi_{2n} - \Psi_n)\big] \tag{133}$$

which gives the same result but with 8- instead of 6-particle correlators. The last two term in the numerator and denominator correlator is called an optimizer. In principle any amount of optimizer can be added to a correlator. In practice there are limitations in computation time, available number of particles per event, etc. The question is will such a transformation increase or decrease the error? For a correlator with l added optimizer terms the error roughly scales

$$\sigma_{v_n} \sim \frac{1}{M^{(2l+m)/2}}\frac{1}{v_n^{2l+m-1}}\,. \tag{134}$$

Since $M > 1$ (can be anywhere from 1 to 2600) and $v_n < 1$ there are two opposing effects. The idea is that if the harmonic used for the optimizer is picked as the highest measured flow coefficient (mostly v_2) and the multiplicity is large, then the error will be suppressed.

A Derivation of Flow Coefficients v_n

Given a 2π-periodic probability density function[30] (p.d.f.) $f(\varphi)$ with sample space $\varphi \in [0, 2\pi)$ one can always represent it formally by its Fourier series (which does not necessarily converge):

$$f(\varphi) = \sum_{n\in\mathbb{Z}} c_n e^{in\varphi}, \qquad c_n = \int_0^{2\pi} f(\varphi) e^{-in\varphi} d\varphi \in \mathbb{C}\,. \tag{135}$$

The expression can be rewritten as

$$f(\varphi) = \sum_{n=-\infty}^{+\infty} c_n e^{in\varphi} = \underbrace{\sum_{n=-\infty}^{1} c_n e^{in\varphi}}_{\sum_{n=1}^{\infty} c_{-n} e^{-in\varphi}} + \sum_{n=1}^{\infty} c_n e^{in\varphi} + c_0 = c_0 + \sum_{n=1}^{\infty} \left(c_{-n} e^{-in\varphi} + c_n e^{in\varphi} \right)\,. \tag{136}$$

A probability density, here $f(\varphi)$, has to be a real function, i.e. $f(\varphi) = f(\varphi)^*$ and therefore the complex Fourier coefficients satisfy

$$c_{-n} = c_n^*\,. \tag{137}$$

Using this, $f(\varphi)$ can again be rewritten as

$$\begin{aligned}
f(\varphi) &= c_0 + \sum_{n=1}^{\infty} \left[c_n e^{in\varphi} + \left(c_n e^{in\varphi} \right)^* \right] && (138)\\
&= c_0 + \sum_{n=1}^{\infty} 2 \cdot \mathfrak{Re} \left(c_n e^{in\varphi} \right) && (139)\\
&\underbrace{=}_{c_n \in \mathbb{C} \Rightarrow c_n = |c_n| e^{i \arg (c_n)}} c_0 + \sum_{n=1}^{\infty} 2 \cdot \mathfrak{Re} \left(|c_n|\, e^{in\varphi + \arg c_n} \right) && (140)\\
&\underbrace{=}_{\substack{\arg c_n \equiv -n\Psi_n \in \mathbb{R} \\ |c_n| \equiv v_n \in \mathbb{R} \\ c_0 \equiv v_0}} v_0 + 2 \sum_{n=1}^{\infty} v_n \mathfrak{Re} \left(e^{in(\varphi - \Psi_n)} \right) && (141)\\
&= v_0 + 2 \sum_{n=1}^{\infty} v_n \cos[n(\varphi - \Psi_n)]\,. && (142)
\end{aligned}$$

Here some redefinitions were applied to match the typically used notation of the field.

---

[30] Which is per definition normalized, but also every function $f(\varphi)$ can w.l.o.g. be normalized: $f_{normal}(\varphi) = \frac{f(\varphi)}{\int f(\varphi)\, d\varphi}$.

Taking the mean, defined by $\langle x\rangle = \int_0^{2\pi} x f(x)dx$, of $\cos\big(n(\varphi - \Psi_n)\big)$ yields:

$$\big\langle \cos[n(\varphi - \Psi_n)]\big\rangle = \int_0^{2\pi} \cos[n(\varphi - \Psi_n)] \cdot f(\varphi)\, d\varphi \tag{143}$$

$$= \int_0^{2\pi} \frac{1}{2}\left(e^{in(\varphi-\Psi_n)} + e^{-in(\varphi-\Psi_n)}\right)\left(v_0 + 2\sum_{m=1}^{\infty} v_m \frac{1}{2}\big(e^{im(\varphi-\Psi_m)} + e^{-im(\varphi-\Psi_m)}\big)\right) d\varphi \tag{144}$$

$$\begin{aligned} = \frac{1}{2}\int_0^{2\pi} & \underbrace{2v_0\left(e^{in(\varphi-\Psi_n)} + e^{-in(\varphi-\Psi_n)}\right)}_{=0} + \\ & + \sum_{m=1}^{\infty} v_m \big[e^{i(n\varphi - n\Psi_n + m\varphi - m\Psi_m)} + e^{-i(n\varphi - n\Psi_n + m\varphi - m\Psi_m)} \\ & + e^{i(n\varphi - n\Psi_n - m\varphi + m\Psi_m)} + e^{-i(n\varphi - n\Psi_n - m\varphi + m\Psi_m)}\big]\, d\varphi \end{aligned} \tag{145}$$

$$\begin{aligned} = \frac{1}{2}\sum_{m=1}^{\infty} v_m \int_0^{2\pi} & \underbrace{e^{i(n+m)\varphi} e^{-i(n\Psi_n + m\Psi_m)}}_{=0} + \underbrace{e^{-i(n+m)\varphi} e^{i(n\Psi_n + m\Psi_m)}}_{=0} \\ & + \underbrace{e^{i(n-m)\varphi} e^{-i(n\Psi_n - m\Psi_m)}}_{=2\pi\delta_{nm} e^{-i(n\Psi_n - m\Psi_m)}} + \underbrace{e^{-i(n-m)\varphi} e^{i(n\Psi_n - m\Psi_m)}}_{=2\pi\delta_{nm} e^{i(n\Psi_n - m\Psi_m)}}\, d\varphi\,. \end{aligned} \tag{146}$$

The integrals over the individual terms are always 0 (because of the 2π symmetry of e^{ix}) except for when $n + m = 0$ or $n - m = 0$. Knowing that the summation indices $n, m \in \mathbb{N}$ ($\mathbb{N}$ without 0), $n + m = 0$ isn't possible. Because of $n - m = 0$ one gets

$$= \frac{1}{2}\sum_{m=1}^{\infty} v_m \left(2\pi\delta_{nm} e^{-i(n\Psi_n - m\Psi_m)} + 2\pi\delta_{nm} e^{i(n\Psi_n - m\Psi_m)}\right) \tag{147}$$

$$= \frac{1}{2} v_n 2\pi \left(\underbrace{e^{-i(n\Psi_n - n\Psi_n)}}_{=1} + \underbrace{e^{i(n\Psi_n - n\Psi_n)}}_{=1}\right) \tag{148}$$

$$= 2\pi v_n\,. \tag{149}$$

The factor of 2π can be canceled with the $\frac{1}{2\pi}$ in v_n (remember: v_n was the Fourier series coefficient $v_n = c_n = \frac{1}{2\pi}\int_0^{2\pi} f(\varphi) e^{-in\varphi}\, d\varphi \in \mathbb{C}$). This is just a matter of defining the Fourier series. In the above part the $\frac{1}{2\pi}$ factor was left inside v_n for shorter equations. During this thesis it we will be pulled out so it cancels.

In summary:

$$f(\varphi) = \sum_{-\infty}^{+\infty} v_n e^{in\varphi} = \frac{v_0}{2\pi} + \frac{1}{\pi}\sum_{n=1}^{\infty} v_n \cos[n(\varphi - \Psi_n)]\,, \tag{150}$$

$$v_n = \big\langle \cos[n(\varphi - \Psi_n)]\big\rangle\,. \tag{151}$$

B Statistical Errors

In this appendix the statistical errors of the flow estimators defined in Eqs. (87) – (94) is derived, however, neglecting covariance terms. Since every event-averaged multiparticle correlator $\langle\langle m\rangle\rangle$ is calculated separately with a separate uncertainty and only at the end combined via Eqs. (87) – (94) to get the final flow estimate, each correlator will be treated as a variable with uncertainty. The uncertainty for the flow estimator is then derived using standard error propagation.

B.1 $v_n\{2\}$

The error of

$$v_n\{2\} = \sqrt{\langle\langle 2\rangle\rangle} \tag{152}$$

is calculated via propagation of uncertainty as

$$\sigma_{v_n\{2\}} = \sqrt{\left(\Delta_{\langle\langle 2\rangle\rangle}\right)^2 \cdot \left(\partial_{\langle\langle 2\rangle\rangle}\sqrt{\langle\langle 2\rangle\rangle}\right)^2} = \frac{\Delta\langle\langle 2\rangle\rangle}{2\sqrt{\langle\langle 2\rangle\rangle}}\,. \tag{153}$$

B.2 $v_n\{4\}$

For

$$v_n\{4\} = \sqrt[4]{-c_n\{4\}} \tag{154}$$

the error can be calculated via propagation of uncertainty:

$$\sigma_{v_n\{4\}} = \sqrt{\left(\Delta_{\langle\langle 2\rangle\rangle}\right)^2 \cdot \left(\partial_{\langle\langle 2\rangle\rangle} f\left(\langle\langle 2\rangle\rangle, \langle\langle 4\rangle\rangle\right)\right)^2 + \left(\Delta_{\langle\langle 4\rangle\rangle}\right)^2 \cdot \left(\partial_{\langle\langle 4\rangle\rangle} f\left(\langle\langle 2\rangle\rangle, \langle\langle 4\rangle\rangle\right)\right)^2}\,, \tag{155}$$

where

$$f\left(\langle\langle 2\rangle\rangle, \langle\langle 4\rangle\rangle\right) = \sqrt[4]{2\langle\langle 2\rangle\rangle^2 - \langle\langle 4\rangle\rangle}\,. \tag{156}$$

That leads to

$$\sigma_{v_n\{4\}} = \frac{\sqrt{16\langle\langle 2\rangle\rangle^2\Delta^2_{\langle\langle 2\rangle\rangle} + \Delta^2_{\langle\langle 4\rangle\rangle}}}{4\left(2\langle\langle 2\rangle\rangle^2 - \langle\langle 4\rangle\rangle\right)^{3/4}}\,. \tag{157}$$

B.3 $v_n\{6\}$

The error of

$$v_n\{6\} = \sqrt[6]{\frac{1}{4}c_n\{6\}} \tag{158}$$

is calculated via

$$\begin{aligned}\sigma_{v_n\{6\}} =& \sqrt{\left(\Delta_{\langle\langle 2\rangle\rangle}\right)^2 \cdot \left(\partial_{\langle\langle 2\rangle\rangle} f\left(\langle\langle 2\rangle\rangle, \langle\langle 4\rangle\rangle, \langle\langle 6\rangle\rangle\right)\right)^2 + \left(\Delta_{\langle\langle 4\rangle\rangle}\right)^2 \cdot \left(\partial_{\langle\langle 4\rangle\rangle} f\left(\langle\langle 2\rangle\rangle, \langle\langle 4\rangle\rangle, \langle\langle 6\rangle\rangle\right)\right)^2} \\ &\overline{+\left(\Delta_{\langle\langle 6\rangle\rangle}\right)^2 \cdot \left(\partial_{\langle\langle 6\rangle\rangle} f\left(\langle\langle 2\rangle\rangle, \langle\langle 4\rangle\rangle, \langle\langle 6\rangle\rangle\right)\right)^2}\end{aligned} \tag{159}$$

where

$$f\left(\langle\langle 2\rangle\rangle, \langle\langle 4\rangle\rangle, \langle\langle 6\rangle\rangle\right) = \sqrt[6]{\frac{1}{4}\left(\langle\langle 6\rangle\rangle - 9\langle\langle 4\rangle\rangle\langle\langle 2\rangle\rangle\right) + 12\langle\langle 2\rangle\rangle^3}\,. \tag{160}$$

This results in

$$\sigma_{v_n\{6\}} = \frac{\sqrt{\Delta^2_{\langle\langle 6\rangle\rangle} + 81\left(16\langle\langle 2\rangle\rangle^4\Delta^2_{\langle\langle 2\rangle\rangle} + \langle\langle 2\rangle\rangle^2\left(\Delta^2_{\langle\langle 4\rangle\rangle} - 8\langle\langle 4\rangle\rangle\Delta^2_{\langle\langle 2\rangle\rangle}\right) + \langle\langle 4\rangle\rangle^2\Delta^2_{\langle\langle 2\rangle\rangle}\right)}}{6\sqrt[3]{2}\left(12\langle\langle 2\rangle\rangle^3 - 9\langle\langle 4\rangle\rangle\langle\langle 2\rangle\rangle + \langle\langle 6\rangle\rangle\right)^{5/6}}\,. \tag{161}$$

B.4 $v_n\{8\}$

The error of

$$v_n\{8\} = \sqrt[8]{-\frac{1}{33}c_n\{8\}} \tag{162}$$

is calculated via the propagation of uncertainty

$$\sigma_{v_n\{8\}} = \sqrt{\left(\Delta_{\langle\langle 2\rangle\rangle}\right)^2 \cdot \left(\partial_{\langle\langle 2\rangle\rangle} f\left(\langle\langle 2\rangle\rangle, \langle\langle 4\rangle\rangle, \langle\langle 6\rangle\rangle, \langle\langle 8\rangle\rangle\right)\right)^2 + \left(\Delta_{\langle\langle 4\rangle\rangle}\right)^2 \cdot \left(\partial_{\langle\langle 4\rangle\rangle} f\left(\langle\langle 2\rangle\rangle, \langle\langle 4\rangle\rangle, \langle\langle 6\rangle\rangle, \langle\langle 8\rangle\rangle\right)\right)^2} \tag{163}$$

$$\overline{+\left(\Delta_{\langle\langle 6\rangle\rangle}\right)^2 \cdot \left(\partial_{\langle\langle 6\rangle\rangle} f\left(\langle\langle 2\rangle\rangle, \langle\langle 4\rangle\rangle, \langle\langle 6\rangle\rangle, \langle\langle 8\rangle\rangle\right)\right)^2 + \left(\Delta_{\langle\langle 8\rangle\rangle}\right)^2 \cdot \left(\partial_{\langle\langle 8\rangle\rangle} f\left(\langle\langle 2\rangle\rangle, \langle\langle 4\rangle\rangle, \langle\langle 6\rangle\rangle, \langle\langle 8\rangle\rangle\right)\right)^2} \tag{164}$$

where

$$f\left(\langle\langle 2\rangle\rangle, \langle\langle 4\rangle\rangle, \langle\langle 6\rangle\rangle, \langle\langle 8\rangle\rangle\right) = \sqrt[8]{-\frac{1}{33}\left(\langle\langle 8\rangle\rangle - 16\langle\langle 6\rangle\rangle\langle\langle 4\rangle\rangle - 18\langle\langle 4\rangle\rangle^2 + 144\langle\langle 4\rangle\rangle\langle\langle 2\rangle\rangle^2 - 144\langle\langle 2\rangle\rangle^4\right)}\,. \tag{165}$$

That leads to the error

$$\begin{aligned}
\sigma_{v_n\{8\}} =& \frac{1}{\sqrt{8\sqrt[8]{33}\left(2\left(-72\langle\langle 4\rangle\rangle\langle\langle 2\rangle\rangle^2 + 8\left(9\langle\langle 2\rangle\rangle^3 + \langle\langle 6\rangle\rangle\right)\langle\langle 2\rangle\rangle + 9\langle\langle 4\rangle\rangle^2\right) - \langle\langle 8\rangle\rangle\right)^{7/8}}} \\
& \times \sqrt{16\left(20736\langle\langle 2\rangle\rangle^6\Delta^2_{\langle\langle 2\rangle\rangle} + 1152\langle\langle 6\rangle\rangle\langle\langle 2\rangle\rangle^3\Delta^2_{\langle\langle 2\rangle\rangle} - 576\langle\langle 4\rangle\rangle\langle\langle 6\rangle\rangle\langle\langle 2\rangle\rangle\Delta^2_{\langle\langle 2\rangle\rangle}\right)} \\
& \overline{+16\left(1296\langle\langle 2\rangle\rangle^4\left(\Delta^2_{\langle\langle 4\rangle\rangle} - 16\langle\langle 4\rangle\rangle\Delta^2_{\langle\langle 2\rangle\rangle}\right) + 16\langle\langle 6\rangle\rangle^2\Delta^2_{\langle\langle 2\rangle\rangle} + 81\langle\langle 4\rangle\rangle^2\Delta^2_{\langle\langle 4\rangle\rangle}\right)} \\
& \overline{+16\left(8\langle\langle 2\rangle\rangle^2\left(2\Delta^2_{\langle\langle 6\rangle\rangle} + 81\langle\langle 4\rangle\rangle\left(8\langle\langle 4\rangle\rangle\Delta^2_{\langle\langle 2\rangle\rangle} - \Delta^2_{\langle\langle 4\rangle\rangle}\right)\right)\right) + \Delta^2_{\langle\langle 8\rangle\rangle}}\,.
\end{aligned} \tag{166}$$

References

[1] H David Politzer, “Reliable Perturbative Results for Strong Interactions?”, *Phys. Rev. Lett.* 30 (1973), pp. 1346–1349.

[2] David J Gross and Frank Wilczek, “Ultraviolet Behavior of Nonabelian Gauge Theories”, *Phys. Rev. Lett.* 30 (1973), pp. 1343–1346.

[3] Michael Edward Peskin and Daniel V. Schroeder, *An introduction to quantum field theory.* Boulder, Col.: Westview Press, 2006.

[4] Thomas Appelquist and W Fischler, “Some Remarks on Van Der Waals Forces in QCD”, *Phys. Lett.* B77 (1978), pp. 405–410.

[5] K A Olive et al., “Review of Particle Physics”, *Chin. Phys.* C38 (2014), p. 90001.

[6] Jihn E. Kim and Gianpaolo Carosi, “Axions and the strong CP problem”, *Rev. Mod. Phys.* 82.1 (Mar. 2010), pp. 557–601.

[7] G Altarelli, “Experimental Tests of Perturbative QCD”, *Annu. Rev. Nucl. Part. Sci.* 39.1 (1989), pp. 357–406.

[8] Kenneth G Wilson, “Confinement of Quarks”, *Phys. Rev.* D10 (1974), pp. 2445–2459.

[9] Helmut Satz, “From Hadrons to Quarks”, *Extrem. States Matter Strong Interact. Phys. An Introd.* Berlin, Heidelberg: Springer Berlin Heidelberg, 2012, pp. 45–63.

[10] Enrico Fermi, “High-energy nuclear events”, *Prog. Theor. Phys.* 5 (1950), pp. 570–583.

[11] R Hagedorn, *Statistical thermodynamics of strong interactions at high-energies.* 1965.

[12] L D Landau, *On the multiparticle production in high-energy collisions.* 1953.

[13] John C Collins and M J Perry, “Superdense Matter: Neutrons Or Asymptotically Free Quarks?”, *Phys. Rev. Lett.* 34 (1975), p. 1353.

[14] N. Cabibbo and G. Parisi, “Exponential hadronic spectrum and quark liberation”, *Phys. Lett. B* 59.1 (1975), pp. 67–69.

[15] Edward V Shuryak, “Theory of hadron plasma”, *Sov. Phys.-JETP (Engl. Transl.);(United States)* 47.2 (1978).

[16] Michael Creutz, “Confinement and the Critical Dimensionality of Space-Time”, *Phys. Rev. Lett.* 43 (1979), pp. 553–556.

[17] J. Kuti, J. Polónyi, and K. Szlachányi, “Monte Carlo study of SU(2) gauge theory at finite temperature”, *Phys. Lett. B* 98.3 (Jan. 1981), pp. 199–204.

[18] M Creutz, “Monte Carlo Study of Quantized SU(2) Gauge Theory”, *Phys. Rev.* D21 (1980), pp. 2308–2315.

[19] Larry D. McLerran and Benjamin Svetitsky, “A Monte Carlo study of SU(2) Yang-Mills theory at finite temperature”, *Phys. Lett. B* 98.3 (Jan. 1981), pp. 195–198.

[20] S.A. Chin, “Transition to hot quark matter in relativistic heavy-ion collision”, *Phys. Lett. B* 78.5 (Oct. 1978), pp. 552–555.

[21] A Chodos et al., “A New Extended Model of Hadrons”, *Phys. Rev.* D9 (1974), pp. 3471–3495.

[22] T Celik, F Karsch, and H Satz, “A PERCOLATION APPROACH TO STRONGLY INTERACTING MATTER”, *Phys. Lett.* B97 (1980), pp. 128–130.

[23] J Cleymans Suhonen, M I Gorenstein, J St?lnacke, and E, "Excluded volume effect and the quark-hadron phase transition", *Phys. Scr.* 48.3 (1993), p. 277.

[24] Lokesh Kumar, *Review of Recent Results from the RHIC Beam Energy Scan.* 2013.

[25] J Wambach, K Heckmann, and M Buballa, *Transport Properties of Strong-Interaction Matter.* 2012.

[26] J. Bardeen, L. N. Cooper, and J. R. Schrieffer, "Theory of superconductivity", *Phys. Rev.* 108.5 (Dec. 1957), pp. 1175–1204.

[27] Mark Alford, Krishna Rajagopal, and Frank Wilczek, "Color-flavor locking and chiral symmetry breaking in high density QCD", *Nucl. Phys. B* 537.1-3 (Jan. 1999), pp. 443–458.

[28] Thomas Schäfer, "Patterns of symmetry breaking in QCD at high baryon density", *Nucl. Phys. B* 575.1-2 (May 2000), pp. 269–284.

[29] Helmut Satz, "The Thermodynamics of Quarks and Gluons", *Phys. Quark-Gluon Plasma Introd. Lect.* Ed. by Sourav Sarkar, Helmut Satz, and Bikash Sinha. Berlin, Heidelberg: Springer Berlin Heidelberg, 2010, pp. 1–21.

[30] A. Bazavov et al., "Equation of state in (2+1)-flavor QCD", *Phys. Rev. D* 90.9 (2014), p. 94503. arXiv: `1407.6387`.

[31] Szabolcs Borsányi et al., "Full result for the QCD equation of state with 2+1 flavors", *Phys. Lett. B* 730 (2014), pp. 99–104.

[32] B. B. Back et al., "The PHOBOS perspective on discoveries at RHIC", *Nucl. Phys. A* 757.1-2 SPEC. ISS. (Aug. 2005), pp. 28–101. arXiv: `0410022 [nucl-ex]`.

[33] I. Arsene et al., "Quark-gluon plasma and color glass condensate at RHIC? The perspective from the BRAHMS experiment", *Nucl. Phys. A* 757.1-2 SPEC. ISS. (Aug. 2005), pp. 1–27. arXiv: `0410020v1 [arXiv:nucl-ex]`.

[34] K. Adcox et al., "Formation of dense partonic matter in relativistic nucleus-nucleus collisions at RHIC: Experimental evaluation by the PHENIX Collaboration", *Nucl. Phys. A* 757.1-2 SPEC. ISS. (Aug. 2005), pp. 184–283. arXiv: `0410003 [nucl-ex]`.

[35] J. Adams et al., "Experimental and theoretical challenges in the search for the quark-gluon plasma: The STAR Collaboration's critical assessment of the evidence from RHIC collisions", *Nucl. Phys. A* 757.1-2 SPEC. ISS. (Aug. 2005), pp. 102–183. arXiv: `0501009 [nucl-ex]`.

[36] Juan Maldacena, "The large N Limit of superconformal field theories and supergravity", *Adv. Theor. Math. Phys.* 2.2 (1998), pp. 231–252. arXiv: `9711200 [hep-th]`.

[37] Edward Witten, "Anti-de Sitter space and holography", *Adv. Theor. Math. Phys.* 2 (1998), p. 253. arXiv: `9802150 [hep-th]`.

[38] S S Gubser, Igor R Klebanov, and Alexander M Polyakov, "Gauge theory correlators from noncritical string theory", *Phys. Lett.* B428 (1998), pp. 105–114. arXiv: `hep-th/9802109 [hep-th]`.

[39] P. K. Kovtun, D. T. Son, and A. O. Starinets, "Viscosity in strongly interacting quantum field theories from black hole physics", *Phys. Rev. Lett.* 94.11 (Mar. 2005), p. 111601. arXiv: `0405231v2 [arXiv:hep-th]`.

[40] G Policastro, D T Son, and A O Starinets, "Shear Viscosity of Strongly Coupled N=4 Supersymmetric Yang-Mills Plasma", *Phys. Rev. Lett.* 87.8 (Aug. 2001), p. 4. arXiv: `0104066 [hep-th]`.

[41] J. Adams et al., "Azimuthal anisotropy in Au+Au collisions at $\sqrt{s_{NN}} = 200\text{GeV}$", *Phys. Rev. C - Nucl. Phys.* 72.1 (July 2005), p. 14904.

[42] A. Adare et al., "Scaling properties of azimuthal anisotropy in Au+Au and Cu+Cu collisions at $sqrts_{NN} = 200\text{GeV}$", *Phys. Rev. Lett.* 98.16 (Apr. 2007), p. 162301. arXiv: `0608033 [nucl-ex]`.

[43] Matthew Luzum and Paul Romatschke, "Conformal relativistic viscous hydrodynamics: Applications to RHIC results at $\sqrt{s_{NN}} = 200$ GeV", *Phys. Rev. C - Nucl. Phys.* 78.3 (Sept. 2008), p. 34915. arXiv: `0804.4015`.

[44] H. Niemi et al., "Influence of shear viscosity of quark-gluon plasma on elliptic flow in ultrarelativistic heavy-ion collisions", *Phys. Rev. Lett.* 106.21 (May 2011), p. 212302. arXiv: `1101.2442`.

[45] Shen Chun, *Sketch of relativistic heavy-ion collisions.* 2014.

[46] Michael Strickland, "Anisotropic hydrodynamics: Three lectures", *Acta Phys. Pol. B* 45.12 (2014), pp. 2355–2393. arXiv: `1410.5786`.

[47] Kohsuke Yagi, Tetsuo Hatsuda, and Yasuo Miake, *Quark-gluon plasma: From big bang to little bang.* Vol. 23. Cambridge University Press, 2005.

[48] F. Gelis, E. Iancu, J. Jalilian-Marian, and R. Venugopalan, "The Color Glass Condensate", *Ann. Rev. Nucl. Part. Sci.* 60 (2010), pp. 463–489. arXiv: `1002.0333`.

[49] T. Lappi and L. McLerran, "Some features of the glasma", *Nucl. Phys. A* 772.3-4 (2006), pp. 200–212. arXiv: `0602189 [hep-ph]`.

[50] Raju Venugopalan, "From glasma to quark–gluon plasma in heavy-ion collisions", *J. Phys. G Nucl. Part. Phys.* 35.10 (2008), p. 104003. arXiv: `0806.1356`.

[51] Rajeev S. Bhalerao, "Relativistic heavy-ion collisions", *Proceedings, 1st Asia-Europe-Pacific Sch. High-Energy Phys.* 2014, pp. 219–239. arXiv: `1404.3294`.

[52] A K Chaudhuri, *A short course on Relativistic Heavy Ion Collisions.* IOPP, 2014. arXiv: `1207.7028 [nucl-th]`.

[53] Raimond Snellings, "Collective Expansion at the LHC: selected ALICE anisotropic flow measurements", *J. Phys.* G41.12 (2014), p. 124007. arXiv: `1408.2532 [nucl-ex]`.

[54] Michael L Miller, Klaus Reygers, Stephen J Sanders, and Peter Steinberg, "Glauber modeling in high energy nuclear collisions", *Ann. Rev. Nucl. Part. Sci.* 57 (2007), pp. 205–243. arXiv: `nucl-ex/0701025 [nucl-ex]`.

[55] J Bartke, *Introduction to Relativistic Heavy Ion Physics.* World Scientific, 2009.

[56] Betty Abelev et al., "Centrality determination of Pb-Pb collisions at $\sqrt{s_{NN}} = 2.76$ TeV with ALICE", *Phys. Rev.* C88.4 (2013), p. 44909. arXiv: `1301.4361 [nucl-ex]`.

[57] Christiane Lefèvre, "The CERN accelerator complex. Complexe des accélérateurs du CERN". Dec. 2008.

[58] Florent Fayette, "Strategies for precision measurements of the charge asymmetry of the W boson mass at the LHC within the ATLAS experiment". PhD thesis. Paris U., VI-VII, 2009. arXiv: `0906.4260 [hep-ex]`.

[59] C Lefevre, "LHC: the guide". Jan. 2008.

[60] Ante Bilandzic, "Anisotropic Flow Measurements in ALICE at the Large Hadron Collider". PhD thesis. 2012.

[61] Alexander Hansen and Jens Jørgen Gaardhøje, "Pseudorapidity dependence of anisotropic azimuthal flow with the ALICE detector". PhD thesis. Copenhagen U., Sept. 2014.

[62] Betty Bezverkhny Abelev et al., "Performance of the ALICE Experiment at the CERN LHC", *Int. J. Mod. Phys.* A29 (2014), p. 1430044. arXiv: `1402.4476 [nucl-ex]`.

[63] K Aamodt et al., "The ALICE experiment at the CERN LHC. A Large Ion Collider Experiment", *J. Instrum.* 3 (2008), S08002. 259 p.

[64] P Cortese et al., "ALICE: Physics performance report, volume I", *J. Phys.* G30 (2004). Ed. by F Carminati et al., pp. 1517–1763.

[65] P Cortese et al., "ALICE: Physics performance report, volume II", *J. Phys.* G32 (2006). Ed. by B Alessandro et al., pp. 1295–2040.

[66] Naomi van der Kolk, "To flow or not to flow: A study of elliptic flow and nonflow in proton-proton collisions in ALICE". PhD thesis. Utrecht U., 2012.

[67] K Aamodt et al., "Alignment of the ALICE Inner Tracking System with cosmic-ray tracks", *JINST* 5 (2010), P03003. arXiv: `1001.0502 [physics.ins-det]`.

[68] Alberica Toia, "Bulk Properties of Pb-Pb collisions at $\sqrt{s_{NN}} = 2.76$ TeV measured by ALICE", *J. Phys.* G38 (2011), p. 124007. arXiv: `1107.1973 [nucl-ex]`.

[69] J Alme et al., "The ALICE TPC, a large 3-dimensional tracking device with fast readout for ultra-high multiplicity events", *Nucl. Instruments Methods Phys. Res. Sect. A Accel. Spectrometers, Detect. Assoc. Equip.* 622.1 (2010), pp. 316–367.

[70] G Dellacasa et al., *ALICE time projection chamber: Technical Design Report.* Technical Design Report ALICE. Geneva: CERN, 2000.

[71] *ALICE Inner Tracking System (ITS): Technical Design Report.* Technical Design Report ALICE. Geneva: CERN, 1999.

[72] Mike Miller and Raimond Snellings, "Eccentricity fluctuations and its possible effect on elliptic flow measurements", (2003). arXiv: `nucl-ex/0312008 [nucl-ex]`.

[73] Sergei A Voloshin, Arthur M Poskanzer, and Raimond Snellings, "Collective phenomena in non-central nuclear collisions", (2008). arXiv: `0809.2949 [nucl-ex]`.

[74] Raimond Snellings, "Elliptic Flow: A Brief Review", *New J. Phys.* 13 (2011), p. 55008. arXiv: `1102.3010 [nucl-ex]`.

[75] Ulrich Heinz and Raimond Snellings, "Collective flow and viscosity in relativistic heavy-ion collisions", *Ann. Rev. Nucl. Part. Sci.* 63 (2013), pp. 123–151. arXiv: `1301.2826 [nucl-th]`.

[76] S Voloshin and Y Zhang, "Flow study in relativistic nuclear collisions by Fourier expansion of Azimuthal particle distributions", *Z. Phys.* C70 (1996), pp. 665–672. arXiv: `hep-ph/9407282 [hep-ph]`.

[77] Ante Bilandzic, Raimond Snellings, and Sergei Voloshin, "Flow analysis with cumulants: Direct calculations", *Phys. Rev.* C83 (2011), p. 44913. arXiv: `1010.0233 [nucl-ex]`.

[78] B Alver and G Roland, "Collision geometry fluctuations and triangular flow in heavy-ion collisions", *Phys. Rev.* C81 (2010), p. 54905. arXiv: `1003.0194 [nucl-th]`.

[79] Zhi Qiu and Ulrich W Heinz, "Event-by-event shape and flow fluctuations of relativistic heavy-ion collision fireballs", *Phys. Rev.* C84 (2011), p. 24911. arXiv: `1104.0650 [nucl-th]`.

[80] Ulrich Heinz, “The smallest of the little bangs – the fluid dynamics of proton-proton and proton-nucleus collisions”, *Symp. Wolfram W. 70th Birthd.* Institute for Advanced Study, Technical University Munich, Garching, 2016.

[81] B Alver et al., “System size, energy, pseudorapidity, and centrality dependence of elliptic flow”, *Phys. Rev. Lett.* 98 (2007), p. 242302. arXiv: `nucl-ex/0610037 [nucl-ex]`.

[82] Sergei A Voloshin, Arthur M Poskanzer, Aihong Tang, and Gang Wang, “Elliptic flow in the Gaussian model of eccentricity fluctuations”, *Phys. Lett.* B659 (2008), pp. 537–541. arXiv: `0708.0800 [nucl-th]`.

[83] Derek Teaney and Li Yan, “Triangularity and Dipole Asymmetry in Heavy Ion Collisions”, *Phys. Rev.* C83 (2011), p. 64904. arXiv: `1010.1876 [nucl-th]`.

[84] Burak Han Alver, Clement Gombeaud, Matthew Luzum, and Jean-Yves Ollitrault, “Triangular flow in hydrodynamics and transport theory”, *Phys. Rev.* C82 (2010), p. 34913. arXiv: `1007.5469 [nucl-th]`.

[85] Rajeev S Bhalerao, Matthew Luzum, and Jean-Yves Ollitrault, “Determining initial-state fluctuations from flow measurements in heavy-ion collisions”, *Phys. Rev.* C84 (2011), p. 34910. arXiv: `1104.4740 [nucl-th]`.

[86] Guang-You Qin, Hannah Petersen, Steffen A Bass, and Berndt Muller, “Translation of collision geometry fluctuations into momentum anisotropies in relativistic heavy-ion collisions”, *Phys. Rev.* C82 (2010), p. 64903. arXiv: `1009.1847 [nucl-th]`.

[87] Li Yan and Jean-Yves Ollitrault, “$\nu_4, \nu_5, \nu_6, \nu_7$: nonlinear hydrodynamic response versus LHC data”, *Phys. Lett.* B744 (2015), pp. 82–87. arXiv: `1502.02502 [nucl-th]`.

[88] Georges Aad et al., “Measurement of the correlation between flow harmonics of different order in lead-lead collisions at $\sqrt{s_{NN}} = 2.76$ TeV with the ATLAS detector”, *Phys. Rev.* C92.3 (2015), p. 34903. arXiv: `1504.01289 [hep-ex]`.

[89] H -J. Drescher and Y Nara, “Effects of fluctuations on the initial eccentricity from the Color Glass Condensate in heavy ion collisions”, *Phys. Rev.* C75 (2007), p. 34905. arXiv: `nucl-th/0611017 [nucl-th]`.

[90] Henri Kowalski and Derek Teaney, “An Impact parameter dipole saturation model”, *Phys. Rev.* D68 (2003), p. 114005. arXiv: `hep-ph/0304189 [hep-ph]`.

[91] J Scott Moreland, Zhi Qiu, and Ulrich W Heinz, “Imprinting Quantum Fluctuations on Hydrodynamic Initial Conditions”, *Nucl. Phys.* A904-905 (2013), pp. 815c–818c. arXiv: `1210.5508 [nucl-th]`.

[92] Alex Kovner, Larry D McLerran, and Heribert Weigert, “Gluon production from nonAbelian Weizsacker-Williams fields in nucleus-nucleus collisions”, *Phys. Rev.* D52 (1995), pp. 6231–6237. arXiv: `hep-ph/9502289 [hep-ph]`.

[93] Alex Krasnitz and Raju Venugopalan, “Nonperturbative computation of gluon mini-jet production in nuclear collisions at very high-energies”, *Nucl. Phys.* B557 (1999), p. 237. arXiv: `hep-ph/9809433 [hep-ph]`.

[94] Alex Krasnitz and Raju Venugopalan, “The Initial energy density of gluons produced in very high-energy nuclear collisions”, *Phys. Rev. Lett.* 84 (2000), pp. 4309–4312. arXiv: `hep-ph/9909203 [hep-ph]`.

[95] T Lappi, “Production of gluons in the classical field model for heavy ion collisions”, *Phys. Rev.* C67 (2003), p. 54903. arXiv: `hep-ph/0303076 [hep-ph]`.

[96] Mikolaj Krzewicki, “Anisotropic flow of identified hadrons in heavy-ion collisions at the LHC”. PhD thesis. 2013.

[97] Fred Cooper and Graham Frye, “Comment on the Single Particle Distribution in the Hydrodynamic and Statistical Thermodynamic Models of Multiparticle Production”, *Phys. Rev.* D10 (1974), p. 186.

[98] Arthur M Poskanzer and S A Voloshin, “Methods for analyzing anisotropic flow in relativistic nuclear collisions”, *Phys. Rev.* C58 (1998), pp. 1671–1678. arXiv: `nucl-ex/9805001 [nucl-ex]`.

[99] Nicolas Borghini, Phuong Mai Dinh, and Jean-Yves Ollitrault, “A New method for measuring azimuthal distributions in nucleus-nucleus collisions”, *Phys. Rev.* C63 (2001), p. 54906. arXiv: `nucl-th/0007063 [nucl-th]`.

[100] Nicolas Borghini, Phuong Mai Dinh, and Jean-Yves Ollitrault, “Flow analysis from multiparticle azimuthal correlations”, *Phys. Rev.* C64 (2001), p. 54901. arXiv: `nucl-th/0105040 [nucl-th]`.

[101] Nicolas Borghini, Phuong Mai Dinh, and Jean-Yves Ollitrault, “Flow analysis from cumulants: A Practical guide”, *Int. Work. Phys. Quark Gluon Plasma Palaiseau, Fr. Sept. 4-7, 2001.* 2001. arXiv: `nucl-ex/0110016 [nucl-ex]`.

[102] Ante Bilandzic et al., “Generic framework for anisotropic flow analyses with multiparticle azimuthal correlations”, *Phys. Rev. C - Nucl. Phys.* 89.6 (June 2014), p. 64904. arXiv: `1312.3572`.

[103] R S Bhalerao, N Borghini, and J Y Ollitrault, “Genuine collective flow from Lee-Yang zeroes”, *Phys. Lett.* B580 (2004), pp. 157–162. arXiv: `nucl-th/0307018 [nucl-th]`.

[104] R S Bhalerao, N Borghini, and J Y Ollitrault, “Analysis of anisotropic flow with Lee-Yang zeroes”, *Nucl. Phys.* A727 (2003), pp. 373–426. arXiv: `nucl-th/0310016 [nucl-th]`.

[105] N Borghini, R S Bhalerao, and J Y Ollitrault, “Anisotropic flow from Lee-Yang zeroes: A Practical guide”, *J. Phys.* G30 (2004), S1213–S1216. arXiv: `nucl-th/0402053 [nucl-th]`.

[106] Ante Bilandzic, Naomi van der Kolk, Jean-Yves Ollitrault, and Raimond Snellings, “Event-plane flow analysis without non-flow effects”, *Phys. Rev.* C83 (2011), p. 14909. arXiv: `0801.3915 [nucl-ex]`.

[107] Sergei A Voloshin, “Toward the energy and the system size dependece of elliptic flow: Working on flow fluctuations”, *22nd Winter Work. Nucl. Dyn. (WWND 2006) La Jolla, California, March 11-19, 2006.* 2006. arXiv: `nucl-th/0606022 [nucl-th]`.

[108] Matthew Luzum and Jean-Yves Ollitrault, “Eliminating experimental bias in anisotropic-flow measurements of high-energy nuclear collisions”, *Phys. Rev.* C87.4 (2013), p. 44907. arXiv: `1209.2323 [nucl-ex]`.

[109] B Alver et al., “Importance of correlations and fluctuations on the initial source eccentricity in high-energy nucleus-nucleus collisions”, *Phys. Rev.* C77 (2008), p. 14906. arXiv: `0711.3724 [nucl-ex]`.

[110] Jean-Yves Ollitrault, Arthur M Poskanzer, and Sergei A Voloshin, “Effect of flow fluctuations and nonflow on elliptic flow methods”, *Phys. Rev.* C80 (2009), p. 14904. arXiv: `0904.2315 [nucl-ex]`.

[111] S Wang et al., “Measurement of collective flow in heavy ion collisions using particle pair correlations”, *Phys. Rev.* C44 (1991), pp. 1091–1095.

[112] P McCullagh and J Kolassa, "Cumulants", *Scholarpedia* 4.3 (2009), p. 4699.

[113] Michael J. Wichura, "Lecture Notes Statistics 304: Distribution Theory". Chicago, 2001.

[114] M Hardy, "Combinatorics of Partial Derivatives", *ArXiv Math. e-prints* (Jan. 2006).

[115] C Ahlbach, J Usatine, and N Pippenger, "A Combinatorial Interpretation of the Joint Cumulant", *ArXiv e-prints* (Nov. 2012). arXiv: `1211.0652 [math.CO]`.

[116] Ryogo Kubo, "Generalized Cumulant Expansion Method", *J. Phys. Soc. Japan* 17.7 (July 1962), pp. 1100–1120.

[117] K Aamodt et al., "Elliptic flow of charged particles in Pb-Pb collisions at 2.76TeV", *Phys. Rev. Lett.* 105 (2010), p. 252302. arXiv: `1011.3914 [nucl-ex]`.

[118] Jaroslav Adam et al., "Anisotropic flow of charged particles in Pb-Pb collisions at $sqrts_{\mathrm{NN}} = 5.02$ TeV", *Phys. Rev. Lett.* 116.13 (2016), p. 132302. arXiv: `1602.01119 [nucl-ex]`.

[119] *ALICE Off-line Framework.*

[120] Jaroslav Adam et al., "Centrality dependence of the charged-particle multiplicity density at midrapidity in Pb-Pb collisions at $\sqrt{s_{\mathrm{NN}}} = 5.02$ TeV", *Phys. Rev. Lett.* 116.22 (2016), p. 222302. arXiv: `1512.06104 [nucl-ex]`.

[121] Betty Bezverkhny Abelev et al., "Multiparticle azimuthal correlations in p-Pb and Pb-Pb collisions at the CERN Large Hadron Collider", *Phys. Rev.* C90.5 (2014), p. 54901. arXiv: `1406.2474 [nucl-ex]`.

[122] Betty Abelev et al., "Anisotropic flow of charged hadrons, pions and (anti-)protons measured at high transverse momentum in Pb-Pb collisions at $\sqrt{s_{NN}} = 2.76$ TeV", *Phys. Lett.* B719 (2013), pp. 18–28. arXiv: `1205.5761 [nucl-ex]`.

[123] Betty Abelev et al., "Centrality dependence of π, K, p production in Pb-Pb collisions at $\sqrt{s_{NN}} = 2.76TeV$", *Phys. Rev.* C88 (2013), p. 44910. arXiv: `1303.0737 [hep-ex]`.

[124] Georges Aad et al., "Measurement of the distributions of event-by-event flow harmonics in lead-lead collisions at $\sqrt{s_{NN}} = 2.76$TeV with the ATLAS detector at the LHC", *JHEP* 11 (2013), p. 183. arXiv: `1305.2942 [hep-ex]`.

[125] Georges Aad et al., "Measurement of event-plane correlations in $\sqrt{s_{NN}} = 2.76$ TeV lead-lead collisions with the ATLAS detector", *Phys. Rev.* C90.2 (2014), p. 24905. arXiv: `1403.0489 [hep-ex]`.

[126] Jiangyong Jia, "Event-shape fluctuations and flow correlations in ultra-relativistic heavy-ion collisions", *J. Phys.* G41.12 (2014), p. 124003. arXiv: `1407.6057 [nucl-ex]`.

[127] Matthew Luzum and Hannah Petersen, "Initial State Fluctuations and Final State Correlations in Relativistic Heavy-Ion Collisions", *J. Phys.* G41 (2014), p. 63102. arXiv: `1312.5503 [nucl-th]`.